Enhancing Long-Haul 15-Mode Fiber Performance: Mode Permutation for Reduced Modal Dispersion

Giammarco Di Sciullo, *Graduate Student Member, IEEE*, Divya A. Shaji, *Graduate Student Member, IEEE*, Menno van den Hout, *Student Member, IEEE*, Georg Rademacher, *Senior Member, IEEE*, Ruben S. Luís, *Senior Member, IEEE*, Benjamin J. Puttnam, *Member, IEEE*, Nicolas K. Fontaine, *Fellow, IEEE, Fellow, Optica*, Roland Ryf, *Fellow, IEEE, Fellow, Optica*, Haoshuo Chen, Mikael Mazur, *Member, IEEE*, David T. Neilson, *Fellow, IEEE*, Pierre Sillard, *Member, IEEE*, Frank Achten, Jun Sakaguchi, *Member, IEEE*, Chigo Okonkwo, *Senior Member, IEEE*, Antonio Mecozzi, *Fellow, IEEE, Fellow, Optica*, Cristian Antonelli, *Senior Member, IEEE, Senior Member, Optica*, and Hideaki Furukawa, *Member, IEEE*

***Abstract*—We explore the efficacy of mode permutation to mitigate the impact of modal dispersion in a 15-mode fiber link for long-haul space-division multiplexed transmission. By introducing strong coupling between all the fiber modes, mode permutation reduces the growth rate of the link's intensity impulse response (IIR) with transmission distance, yielding a reduction in the receiver MIMO-DSP complexity. Using a recirculating fiber-loop configuration, we experimentally compare four permutation schemes and find that they are similarly effective in reducing the increase of the IIR duration from proportional to the square-root of propagation distance. At the reach of 530 km – the largest achievable with the time-domain MIMO window of 71.4 ns available in the experiment in the absence of mode permutation – the IIR duration is seen to reduce from almost 40 ns to less than 15 ns, while the maximum reach achieved with the use of mode permutation increases to 1178 km. We also devise a simple model to simulate propagation in realistic MMF links with independent fiber spans, whose parameters can be conveniently extracted from the data. In achieving good agreement between the simulated and experimental results, the model suggests that the effectiveness of mode permutation in a realistic 15-mode fiber link, composed of independent fiber spans, is only slightly greater than in the experimental recirculating-loop configuration.**

***Index Terms*—Modal dispersion, multi-mode fiber transmission, mode permutation, space-division multiplexing.**

Received 12 April 2024; revised 29 July 2024 and 27 August 2024; accepted 30 August 2024. This work was supported in part by Italian Government through INCIPICT and FIRST Projects and in part by KPN-TU/e Smart Two Program and European Union's Horizon Europe Research and Innovation Programme under the Marie Sklodowska- Curie Grant Agreement Number 101072409. *(Corresponding author: Giammarco Di Sciullo.)*

Giammarco Di Sciullo is with the Photonic Network System Laboratory, National Institute of Information and Communications Technology, Tokyo 184-8795, Japan, and also with the University of L'Aquila and CNIT, 67100 L'Aquila, Italy (e-mail: giammarco.disciullo@graduate.univaq.it).

Divya A. Shaji, Antonio Mecozzi, and Cristian Antonelli are with the University of L'Aquila and CNIT, 67100 L'Aquila, Italy (e-mail: divyaann.shaji@univaq.it; antonio.mecozzi@univaq.it; cristian.antonelli@univaq.it).

Menno van den Hout is with the Photonic Network System Laboratory, National Institute of Information and Communications Technology, Tokyo 184-8795, Japan, and also with the High Capacity Optical Transmission Laboratory, Electro-Optical Communications Group, Eindhoven University of Technology, 5600MB Eindhoven, The Netherlands (e-mail: m.v.d.hout@tue.nl).

Georg Rademacher is with the Photonic Network System Laboratory, National Institute of Information, and Communications Technology, Tokyo 184-8795, Japan. He is now with the Institute of Electrical and Optical Communications, University of Stuttgart, 70174 Stuttgart, Germany (e-mail: georg.rademacher@int.uni-stuttgart.de).

Ruben S. Luís, Benjamin J. Puttnam, Jun Sakaguchi, and Hideaki Furukawa are with the Photonic Network System Laboratory, National Institute of Information and Communications Technology, Tokyo 184-8795, Japan (e-mail: rluis@nict.go.jp; ben@nict.go.jp; jsakaguchi@nict.go.jp; furukawa@nict.go.jp).

Nicolas K. Fontaine, Roland Ryf, Haoshuo Chen, Mikael Mazur, and David T. Neilson are with Nokia Bell Labs, New Providence, NJ 07974 USA (e-mail: nicolas.fontaine@nokia-bell-labs.com; roland.ryf@nokia-bell-labs.com; haoshuo.chen@nokia-bell-labs.com; mikael.mazur@nokia-bell-labs.com; david.neilson@nokia-bell-labs.com).

Pierre Sillard is with Prysmian Group, 62092 Haisnes Cedex, France (e-mail: pierre.sillard@prysmiangroup.com).

Frank Achten is with Prysmian Group, 5651 CA Eindhoven, The Netherlands (e-mail: frank.achten@prysmiangroup.com).

Chigo Okonkwo is with the High Capacity Optical Transmission Laboratory, Electro-Optical Communications Group, Eindhoven University of Technology, 5600MB Eindhoven, The Netherlands (e-mail: c.m.okonkwo@tue.nl).

Color versions of one or more figures in this article are available at https://doi.org/10.1109/JLT.2024.3453553.

Digital Object Identifier 10.1109/JLT.2024.3453553

I. Introduction

As DEMAND for higher data rates is expected to continue its exponential increase in optical fiber networks, and single-mode optical fibers are reaching their transmission limits [1], space-division multiplexing (SDM) has gained traction as a promising alternative to address the impending capacity crunch [2]. Proposed SDM fibers include multi-core fibers (MCFs), multi-mode fibers (MMFs) and hybrid multi-core multi-mode fibers (MC-MMFs) [3]. Specifically, MMFs, wherein discrete data signals are multiplexed across distinct spatial modes can support a substantial quantity of spatial channels within the same 125 μm cladding diameter as standard single-mode fibers (SMFs). This characteristic ensures similar fiber mechanical reliability and compatibility with current cabling and manufacturing processes [4]. Nonetheless, the accumulation of modal dispersion (MD) has a direct impact on the required memory length for the multiple-input multiple-output (MIMO) equalizer [5], imposing constraints on both mode count and transmission reach. Indeed, while short-distance transmission utilizing MMFs with up to 55 modes has been recently reported [6],

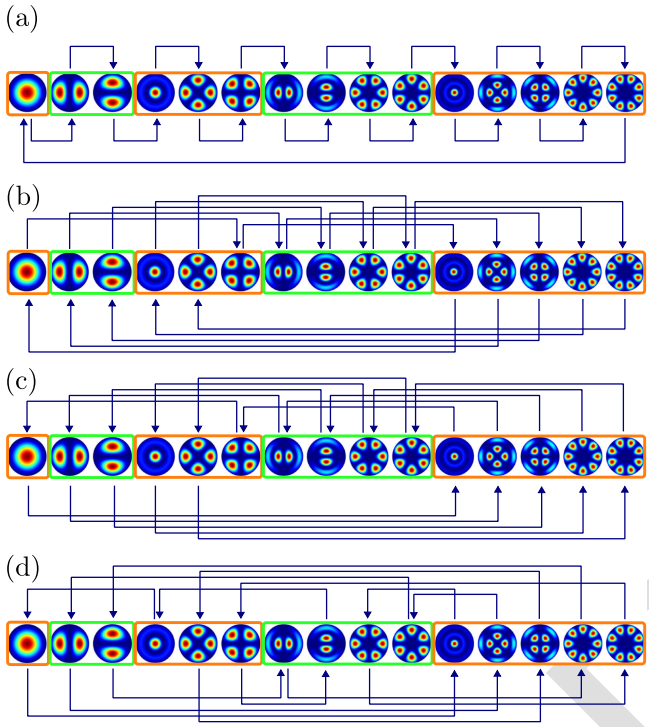

Fig. 1. Sketch of the considered mode permutation schemes: (a) C-MP, (b) Clockwise C-MGP, (c) Counter-clockwise C-MGP and (d) NC-MGP.

[7], [8], experiments targeting long-haul transmission have only used up to 15 fiber modes [9], [10], [11], [12], [13], [14], [15]. In addressing the accumulation of MD, a strategic approach involves intentionally inducing strong mode coupling within the MMF link. This method is grounded in the understanding that modal dispersion increases proportionally to the square root of the propagation distance under conditions of strong mode mixing, as opposed to a proportional increase with propagation distance in situations marked by no-to-weak mode coupling [16], [17], [18]. In pursuit of robust mode coupling to counteract the accumulation of MD, a practical implementation involves the incorporation of lumped mode scramblers along the fiber link. This method stands as a viable scheme, strategically implemented to enhance mode mixing and mitigate MD effects, offering a solution to optimize the performance of the MMF link [18]. It is scalable for arbitrary mode counts, thereby providing a practical approach for future MMF system deployments. Recent advancements in this scheme include the proposals of cyclic mode permutation (C-MP) and cyclic mode-group permutation (C-MGP), demonstrating evolving techniques to further refine and improve the effectiveness of the mode coupling strategy [9], [10], [11], [12], [13].

In this work we examine the efficacy of four distinct mode permutation (MP) schemes within a recirculating-loop-based, long-haul 15-mode fiber link, expanding on [19]. Employing these permutation schemes allowed extending the transmission reach from 530 km to 1178 km while significantly reducing the complexity of the receiver MIMO digital signal processing (DSP). Notably, at 530 km, there was a reduction exceeding 65% in the duration of the MMF link intensity impulse response (IIR). An important supplement to the original work in [19] is the study of mode-dependent loss (MDL) in the MMF system, which shows that MP does not affect MDL accumulation with transmission distance. We also developed a simple model for the simulation of multi-mode propagation to assess the effectiveness of MP in realistic links with independent fiber spans, as opposed to the recirculating-loop scheme used in the experiment. The model relies on a handful of parameters that can be conveniently extracted from the experimental data. Despite its simplicity, the model demonstrated accuracy in reproducing the experimental results. Numerical results obtained for a link composed of independent fiber spans showed only a modest improvement in the performance of MP compared to the recirculating-loop configuration, further supporting the reliability and applicability of the experimental findings. Finally, the model was used to explain the observed independence of MDL accumulation on MP.

The remainder of this paper is organized as follows. Section II delves into the concept of mode permutation and introduces the schemes examined in the experiment. Section III outlines the experimental setup and presents the obtained results. In Section IV, a simulation framework complementing the experimental results is introduced and the corresponding findings are presented. The conclusions of this work are drawn in Section V.

II. Mode Permutation Schemes

Graded-index-core multi-mode fibers are characterized by the existence of non-degenerate mode groups, such that modes within the same group couple strongly during propagation, whereas modes belonging to different groups are weakly coupled and the extent to which they mix increases with propagation distance. In short-reach applications, where the inter-mode-group coupling is negligible, the individual mode groups can be addressed independently with a considerable simplification of the receiver MIMO [20], [21]. However, in metro-to-long-haul applications that are of interest for this work, a full-MIMO approach (where all the fiber modes are processed jointly) becomes necessary, in spite of the fact that non-degenerate mode groups may remain only partially coupled. In this regime MD, which is typically quantified in terms of the link's IIR duration, increases linearly with propagation distance at first, transiting to some sub-linear growth when inter-mode-group coupling becomes substantial. The complexity of the receiver MIMO-DSP grows accordingly. In this scenario, strong coupling between all modes is preferred. In fact, in the regime of strong mode mixing, MD is known to grow only proportionally to the square root of propagation distance [16], [17], [18], implying a drastic reduction in the MIMO-DSP complexity compared to the regime of partial mode coupling.

A practical approach to induce strong coupling between modes belonging to different groups involves the introduction of lumped mode scramblers along the MMF link. In this study, we investigate the effectiveness of four distinct MP schemes in introducing strong mode mixing along a multi-span MMF link, where MP is implemented through a de-multiplexer/multiplexer (De-MUX/MUX) device pair at the end of each span. The first

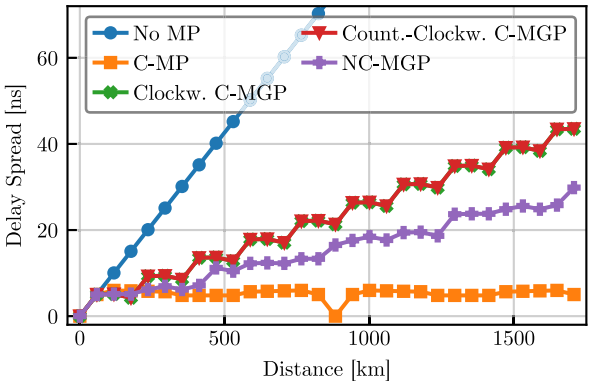

Fig. 2. Delay spread versus propagation distance in the absence of mode coupling in the MMF spans, with and without MP, as obtained through numerical simulation.

device serves to separate the multi-mode field at the output of the MMF into individual single-mode fields. These are subsequently cross-connected to the single-mode sections of the recirculating loop, which guide the signal back to the input of the second device. Fig. 1 illustrates the mode permutation schemes under consideration for the 15-mode fiber used in the experiment. The first scheme [9] (Fig. 1(a)), employs unitary C-MP. In this method, the 15 spatial modes undergo a cyclic shift, moving one position towards higher-order modes at each permutation stage. The second [12], [13] and third schemes, involve the cyclic clockwise (clockwise C-MGP, Fig. 1(b)) and counter-clockwise (counter-clockwise C-MGP, Fig. 1(c)) shifts of the 15 spatial modes by five positions, corresponding to the largest mode-group size. These schemes exhibit a periodic pattern, where spatial modes revert to their initial configuration after either 15 or 3 permutation stages, respectively. Introducing a novel approach in our work [19], the fourth scheme (Fig. 1(d)), referred to as non-cyclic mode-group permutation (NC-MGP), breaks away from periodicity by implementing controlled inter-mode-group permutation. In this scheme, spatial modes within a given mode group are mapped onto other spatial modes of the remaining mode groups, with careful consideration to minimize multiple mappings between any two mode groups. We note that the proposed scheme is one of the many possible schemes that are non-periodic for practical numbers of recirculations. Additionally, the proposed approach can easily be generalized to construct non-cyclic permutation schemes for multi-mode fibers supporting arbitrary number of modes.

It is instructive noting that in the ideal case where no coupling occurs during propagation in the MMF spans, the C-MP scheme would be optimal in terms of delay management. This is illustrated in Fig. 2, where we plot the *delay spread* (that is, the largest differential delay between any two modes) versus propagation distance both in the absence of MP and for each of the considered permutation schemes, under the assumption of uncoupled MMF propagation. For the plot we assumed numerical values extracted from the experiment. In particular, we assumed a 15-mode fiber link with a span length of 58.9 km and the differential mode-group delays (DMGDs) relative to the fundamental mode measured at 1557.8 nm. These are listed

TABLE I
DISPERSION COEFFICIENTS AT 1557.8 NM USED FOR SIMULATION

	$\mathbf{MG}_a$	$\mathbf{MG}_b$	$\mathbf{MG}_c$	$\mathbf{MG}_d$	$\mathbf{MG}_e$
MD γ_u (ps/km$^{1/2}$)	2.1369	13.304	8.0916	9.8246	16.952
DMGD β'_u (ps/km) (w.r.t. $\mathbf{MG}_a$)	–	−85.236	−67.219	−54.399	−68.951

in Table I, which is discussed in Section IV, along with other parameters that are not used in this section. The plot shows that, as expected, in the absence of MP the delay spread grows linearly with propagation distance (blue dots), and it coincides with the differential delay between the slowest and the fastest modes. In the case of C-MGP (crosses and triangles) and NC-MGP (plus symbols), it also grows linearly with propagation distance, yet with a lower growth rate. In contrast, the delay spread is bounded and periodic in the case of C-MP (squares), as a result of the fact that each mode accumulates the same propagation delay after a number of permutation stages equal to the number of modes.

This picture changes completely in the presence of random mode coupling. Indeed, the experimental and simulation results presented in the following sections show that in realistic regimes of intra-group and inter-group coupling all permutation schemes have similar performance. In simulations, the C-MP scheme is even slightly lower performing than the others, which aligns with the observation that this scheme is the least effective in enhancing inter-mode-group coupling, as it only couples a single mode of each group into a mode of an adjacent mode group.

III. EXPERIMENT

A. Experimental Setup

Fig. 3 illustrates the experimental setup employed to validate the efficacy of the examined mode permutation schemes. To generate a three-channel sliding test band, carriers from three tunable lasers (TLs) were modulated using two dual-polarization IQ-modulators (DP-IQMs). These modulators were driven by the same 65 GS/s 4-channel arbitrary waveform generator (AWG). The resulting modulated signals adopted the form of dual-polarization quadrature phase-shift keying (DP-QPSK) signals with a 1% roll-off root-raised cosine pulse shape, transmitted at a rate of 24.5 GBd. A dummy-band was generated by utilizing an optical processor (OP) to spectrally flatten the amplified spontaneous emission noise originating from an erbium-doped fiber amplifier. The composite signal, encompassing both the test and dummy bands, was passed through a loading acousto-optic modulator (AOM), acting as an optical switch, before undergoing a split and delay procedure to generate 15 uncorrelated replicas of the same signal. These replicas, characterized by a relative delay of 150 ns, were subsequently directed into 15 parallel recirculating loops with precisely aligned path lengths. The alignment of the 15 parallel recirculating loops was executed with a precision within the tolerance range of ± 1 cm, corresponding to a differential offset on the order of approximately ± 50 ps. The signals associated with each of the 15 loops were amplified and subsequently multiplexed using a multi-plane light converter (MPLC) [22].

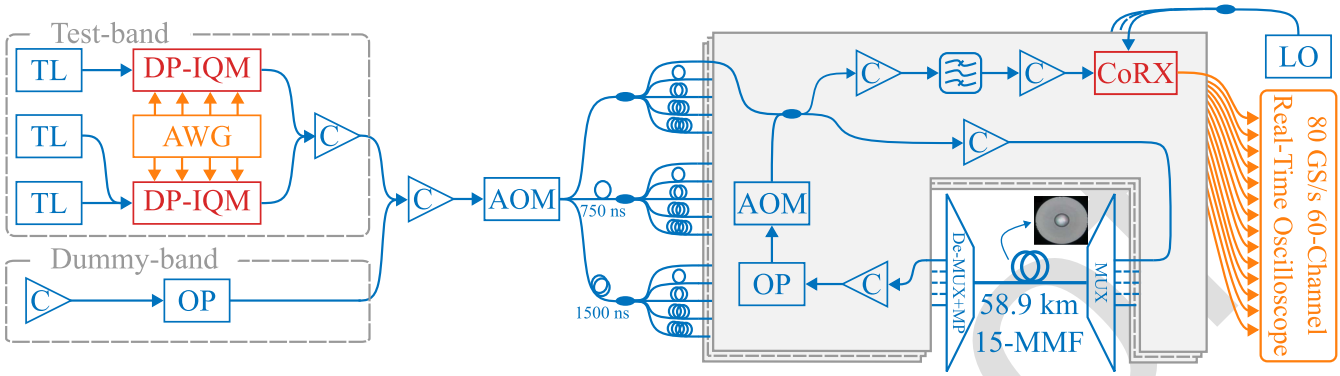

Fig. 3. Experimental setup of the recirculating-loop-based long-haul 15-mode fiber link. Mode permutation is performed at the de-multiplexing stage.

Following the multiplexing process, the combined signal was launched into a 58.9 km long span of 15-mode MMF with low loss (between 0.21 dB/km and 0.24 dB/km for the 15 spatial modes at 1550 nm) and inherently low DMGD (<100 ps/km at 1550 nm) [23]. The outputs of the MPLC de-multiplexer were connected to the single-mode loops based on the prescribed permutation schemes. Subsequently, the signals entered a second amplification stage, followed by OPs to rectify amplifier gain tilts as well as fiber and component loss profiles, and looping AOMs to implement recirculating-loop transmission. Regarding signal reception, the 15 outputs from the parallel loops were first amplified. Subsequently, the channel of interest (COI) was filtered and amplified once more before being received by 15 coherent receivers (CoRXs) that shared a common path-length aligned local oscillator (LO). The electrical signals were captured using an 80-GS/s 60-channel real-time oscilloscope, with the recorded traces intended for offline DSP, mainly involving a time-domain 30 × 30 MIMO equalizer. This required a time-domain equalizer window of 71.4 ns in the absence of MP, and of only 38.8 ns when MP was present in the case of recirculating-loop transmission.

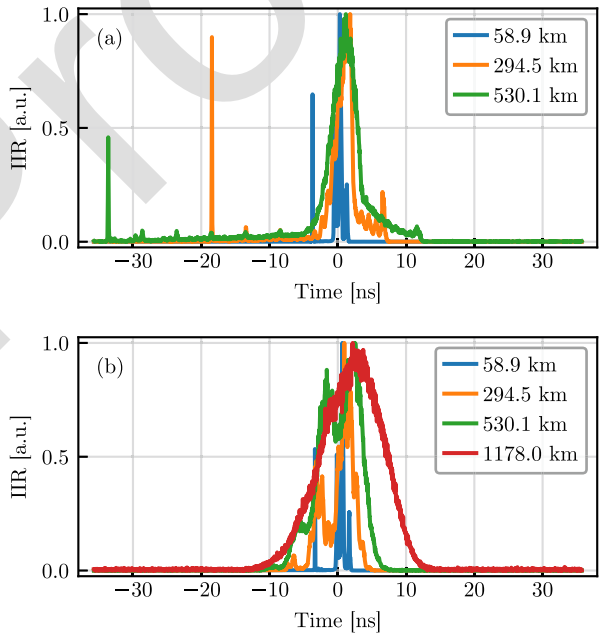

Fig. 4. Intensity impulse response for various transmission distances at 1557.8 nm (a) in the absence of MP and (b) with NC-MGP.

B. Experimental Results

1) Modal Dispersion Accumulation: Fig. 4(a) and (b) show how the shape of the IIR measured at 1557.8 nm evolves as propagation distance increases in the absence of MP and when NC-MGP is applied, respectively. Here, the IIR is defined as the sum of the absolute square values of the equalizer taps, normalized with respect to their maximum value. The isolated peaks seen in the first case are an indication of weak inter-group coupling occurring in the MMF spans, while their disappearance after a few spans in the second case is clearly a consequence of MP. Moreover, the Gaussian-shaped profile of the IIR at 1178 km is a signature of the strong mode coupling regime achieved in the presence of MP [17], [24].

In Fig. 5(a) we plot the duration of the IIR versus propagation distance for all permutation schemes, as well as in the absence of MP. Here, we define the IIR duration as the time interval encompassing 98% of the IIR energy, and each data point is obtained by averaging the IIR duration of the MMF link across five different wavelength channels spanning the C-band, specifically at 1533.9, 1539.8, 1545.7, 1553.7, and 1557.8 nm. The dots are obtained in the absence of MP and the straight line is a linear fit to the data, showing that in this case the IIR duration starts increasing linearly with propagation distance, as a result of the weak inter-mode-group coupling.[1] As inter-group coupling becomes non-negligible, a transition to a sub-linear growth of the IIR duration is seen, at approximately 400 km. The markers, complemented by a square-root data fit growing at a rate of approximately 496 ps/$\sqrt{\text{km}}$, refer to the considered permutation schemes. The remarkable alignment between the data and the square-root fit indicates that the MMF link is operating in the strong mode coupling regime, underscoring

[1]We acknowledge that the observed linear increase in the IIR duration with propagation distance, in the absence of mode permutation, may be attributed in part to certain loop artifacts–such as path-length misalignment between single-mode loops–that are inherently present in practical transmission systems. If this assumption holds true, our findings demonstrate the effective mitigation of these artifacts' impact through the implementation of mode permutation.

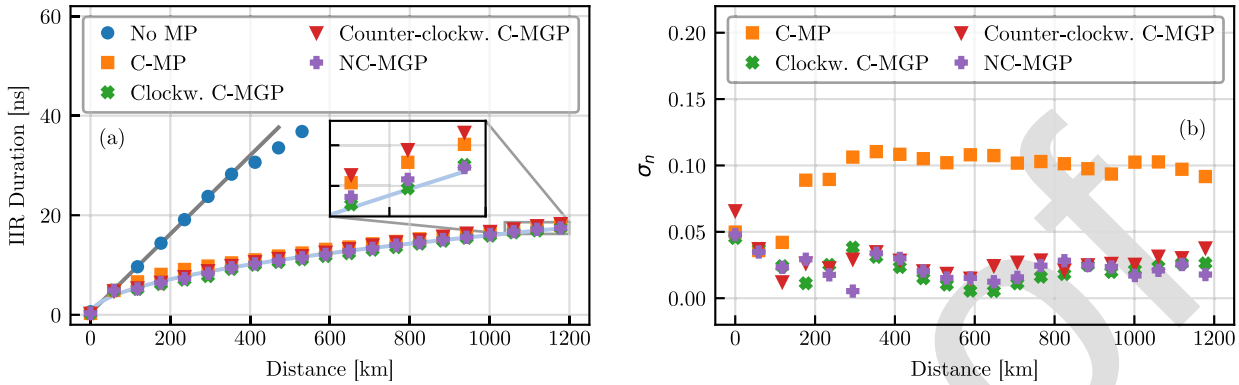

Fig. 5. (a) Wavelength-averaged IIR duration versus transmission distance in the absence of MP and for the considered permutation schemes and (b) normalized standard deviation of the IIR duration versus transmission distance for the considered permutation schemes. The line spacing in the inset of (a) is 2 ns.

the efficacy of the considered permutation schemes in facilitating inter-mode-group coupling. The performance among the schemes exhibits no significant differences, while an impressive reduction of approximately 65% in the IIR duration is obtained at 530.1 km. The fact that C-MP performs similar to the other schemes is in contrast with what was observed in [10]. We attribute this discrepancy to the fact that, in our case, C-MP always maps LP_{01} into LP_{11}, which are the fastest and the slowest mode groups,[2] respectively, at all wavelengths used in the experiment, therefore implementing a delay-management scheme that remains somewhat effective also in the presence of random mode coupling, beyond the ideal case of no-coupling illustrated in Fig. 2. However, this result would change if the first and the second mode groups were not the fastest and the slowest, respectively.

We also examined the wavelength dependence of the IIR duration. To this end, we calculated the normalized standard deviation of the IIR duration measured across the five distinct wavelength channels spanning the C-band for each permutation scheme. This is obtained by normalizing the actual standard deviation of the IIR duration with respect to its average value, namely $\sigma_n = \frac{1}{\mu}\sqrt{\frac{1}{N_{\text{ch}}}\sum_{i=1}^{N_{\text{ch}}}(T_i-\mu)^2}$, where T_i is the i-th wavelength-channel's IIR duration, and $\mu = \frac{1}{N_{\text{ch}}}\sum_{i=1}^{N_{\text{ch}}} T_i$ is the average duration across all channels. In Fig. 5(b), σ_n is plotted versus propagation distance for each permutation scheme. The plot shows that all permutation schemes have similar wavelength dependence,[3] with the exception of the C-MP scheme, which exhibits a stronger dependence on wavelength. We speculate that the larger deviation is due to the fact that the C-MP scheme is less effective in achieving strong mode coupling than the other schemes, which makes the profile and duration of the IIR not as deterministic as it would be expected [17].

2) MDL Accumulation: Modal dispersion is a unitary effect with no direct implications on the achievable data transmission capacity. In contrast, MDL is non-unitary and it fundamentally limits the achievable transmission performance [26], [27], [28],

[2]For the channel at 1558.8 nm, this can be seen in Table I.

[3]Specifically, in [25], the IIR duration is seen to increase as a function of wavelength.

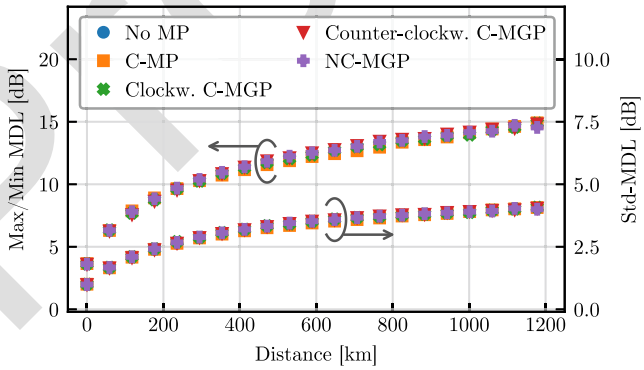

Fig. 6. Wavelength-averaged Max/Min MDL and Std-MDL versus propagation distance in the absence of MP and for the considered permutation schemes.

[29]. We characterize the link's MDL by using two metrics. The first metric is the ratio in dB between the largest and smallest eigenvalues of $\mathbf{H}(\omega)\mathbf{H}^{\dagger}(\omega)$, where by $\mathbf{H}(\omega)$ we denote the frequency-dependent transfer matrix of the MMF link and by $\mathbf{H}^{\dagger}(\omega)$ its hermitian adjoint. We refer to this metric as Max/Min MDL. The frequency-dependent transfer matrix $\mathbf{H}(\omega)$ is derived as the inverse of the Fourier transform of the time-domain MIMO equalization matrix. The second metric is the standard deviation of the natural logarithm of all of the eigenvalues of the same matrix, also expressed in dB [27]. We refer to this metric as Std-MDL. The frequency dependence of the so-evaluated quantities is then eliminated by performing a frequency average across the WDM channel bandwidth.

In Fig. 6, we plot the MDL of the 15-mode fiber link versus propagation distance for all the considered permutation schemes, as well as in the absence of MP. It is worth noting that the results in the absence of MP are hidden by the presence of the other data points. Similarly to what was done for the IIR duration, each data point is obtained by averaging the MDL of the MMF link across the five channel wavelengths. The vertical axis on the left refers to the Max/Min MDL, while the vertical axis on the right refers to the Std-MDL. The results in the latter figure show no substantial differences among the various permutation scenarios, indicating that MP does not affect the accumulation of MDL, in agreement with what was observed

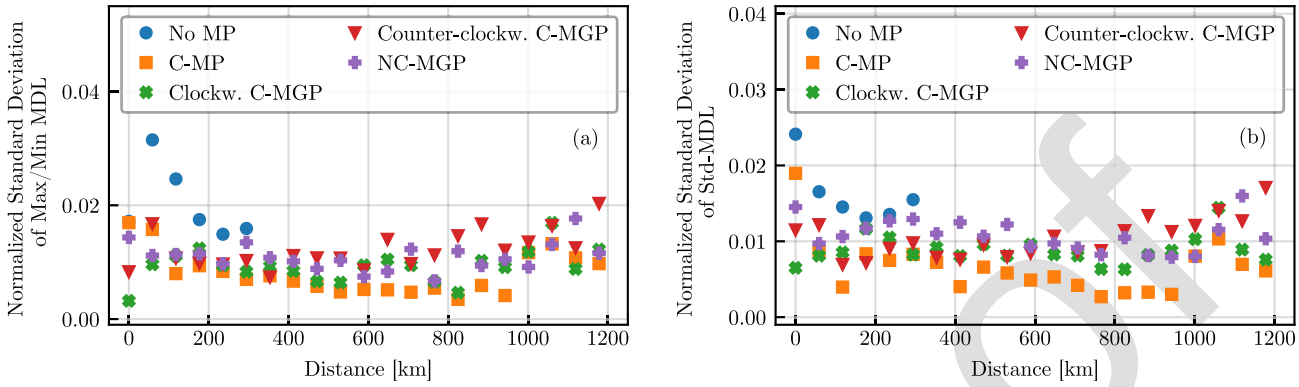

Fig. 7. Normalized standard deviation of (a) Max/Min MDL and (b) Std-MDL versus transmission distance in the absence of MP and for the considered permutation schemes.

in [30]. An interesting feature that emerges from the results of Fig. 6 is that MDL accumulates proportionally to the square root of propagation distance not only in the presence of MP, but also when no MP is implemented. This result comes as a surprise, as one would expect to see a linear growth of MDL with propagation distance. A possible explanation of this behavior is that MDL is dominated by some intra-mode-group MDL, possibly arising from the in-span fiber splices, rather than by inter-mode-group MDL. In particular, we have verified that the MDL values extracted from the channel-transfer-matrix blocks describing the fourth and fifth mode groups after one fiber span are comparable in magnitude to the overall MDL. On the other hand, MDL measurements performed on a deployed 48 km-long fiber of the same kind used in this work have shown that when addressing only the fourth fiber mode-group [31] or all the fiber modes [32], the measured MDL values are quite similar. These evidences provide a qualitative explanation of why MDL grows proportionally with the square root of propagation distance, namely because its accumulation is dominated by strong coupling within a group of quasi-degenerate modes.

We also characterized the wavelength dependence of MDL. To this end, we computed the normalized standard deviation of the MDL measured across the five distinct wavelength channels spanning the C-band for each permutation scheme. Fig. 7 shows the resulting values of the normalized standard deviation plotted versus the transmission distance in the absence of MP and for all the considered permutation schemes, with Fig. 7(a) referring to the Max/Min MDL, and Fig. 7(b) to the Std-MDL. The absence of substantial difference between the considered scenarios is consistent with the argument that MDL accumulation is dominated by intra-mode-group dynamics.

IV. Simulations

In this section we perform simulations in support of the experimental results, with two main goals. On the one hand, we aim to assess whether the similarity in performance between the considered permutation schemes is consistent with some simple and fully-controllable model or results from practical implementation aspects. On the other hand, we aim to assess whether the performance of MP improves in real systems, where the signal propagates in uncorrelated fiber spans, as compared to the case where it propagates in the same fiber span in a recirculating-loop configuration.

A. Model for Distributed Coupling and Parameter Extraction

We start by considering two non-degenerate mode groups a and b, which we describe by means of generalized Jones vectors $\vec{E}_a$ and $\vec{E}_b$ [16], whose evolution along the fiber obeys the following set of coupled equations,

$$\frac{\mathrm{d}\vec{E}_a}{\mathrm{d}z} = i\beta_a\vec{E}_a + i\omega\beta'_a\vec{E}_a + i\frac{\vec{V}_a\cdot\vec{\Lambda}_a}{2N_a}\vec{E}_a + i\omega\frac{\vec{W}_a\cdot\vec{\Lambda}_a}{2N_a}\vec{E}_a - \frac{\alpha_a}{2}\vec{E}_a - \frac{\vec{\alpha}_a\cdot\vec{\Lambda}_a}{2} + i\mathbf{C}\vec{E}_b \quad (1)$$

$$\frac{\mathrm{d}\vec{E}_b}{\mathrm{d}z} = i\beta_b\vec{E}_b + i\omega\beta'_b\vec{E}_b + i\frac{\vec{V}_b\cdot\vec{\Lambda}_b}{2N_b}\vec{E}_b + i\omega\frac{\vec{W}_b\cdot\vec{\Lambda}_b}{2N_b}\vec{E}_b - \frac{\alpha_b}{2}\vec{E}_b - \frac{\vec{\alpha}_b\cdot\vec{\Lambda}_b}{2} + i\mathbf{C}^\dagger\vec{E}_a. \quad (2)$$

Here β_u and β'_u, with $u\in\{a,b\}$, are the propagation constant and its derivative with respect to the angular frequency ω, respectively, for mode group u, while N_u is the number of degenerate spatial modes in the same group. By $\vec{V}_u$ we denote a generalized Stokes vector of dimension $D_u = 4N_u^2-1$, while by $\vec{\Lambda}_u$ we denote a vector whose elements are $2N_u\times 2N_u$ generalized Pauli matrices, so that $\vec{V}_u\cdot\vec{\Lambda}_u = \sum_{n=1}^{D_u} V_{u,n}\Lambda_{u,n}$ [16]. This term describes intra-group random mode coupling in mode groups u. The vector $\vec{W}_u$ is also a generalized Stokes vector and it describes intra-group modal dispersion [16]. The matrix $\mathbf{C}$ and its Hermitian adjoint $\mathbf{C}^\dagger$ account for random inter-group coupling. By α_a and α_b we denote the mode-group averaged loss coefficients, while the vectors $\vec{\alpha}_a$ and $\vec{\alpha}_b$ are the local MDL vectors, which we also model as independent white-noise processes of suitable strength [28]. In what follows, we model both intra-group and inter-group random coupling by means of white noise processes, with the result that the mismatch in propagation constant becomes immaterial and the terms proportional to β_u can be dropped [33]. A further simplification is obtained by establishing a reference frame that

follows intra-group coupling in each mode group. This yields the following simplified equations

$$\frac{\mathrm{d}\vec{E}_a}{\mathrm{d}z} = i\omega\beta'_a\vec{E}_a + i\omega\frac{\vec{W}_a\cdot\vec{\Lambda}_a}{2N_a}\vec{E}_a - \frac{\alpha_a}{2}\vec{E}_a - \frac{\vec{\alpha}_a\cdot\vec{\Lambda}_a}{2} + i\mathbf{C}\vec{E}_b \tag{3}$$

$$\frac{\mathrm{d}\vec{E}_b}{\mathrm{d}z} = i\omega\beta'_b\vec{E}_b + i\omega\frac{\vec{W}_b\cdot\vec{\Lambda}_b}{2N_b}\vec{E}_b - \frac{\alpha_b}{2}\vec{E}_b - \frac{\vec{\alpha}_b\cdot\vec{\Lambda}_b}{2} + i\mathbf{C}^\dagger\vec{E}_a, \tag{4}$$

with

$$\langle W_{u,i}(z)W_{u,j}(z')\rangle = \gamma_u^2\delta_{i,j}\delta(z-z') \tag{5}$$

$$\langle \alpha_{u,i}(z)\alpha_{u,j}(z')\rangle = \zeta_u^2\delta_{i,j}\delta(z-z') \tag{6}$$

$$\langle C_{i,j}(z)C^*_{i',j'}(z')\rangle = \eta^2\delta_{i,i'}\delta_{j,j'}\delta(z-z') \tag{7}$$

$$\langle C_{i,j}(z)C_{i',j'}(z')\rangle = 0, \tag{8}$$

where the coefficients involved are to be extracted from the experimental data. The inverse group velocities β'_u are obtained by inspecting the peaks of the measured IIR after propagation in the first fiber span.

The MD coefficients γ_u^2 are known to be related to the duration of the intra-group intensity impulse responses through the relation $T_u^2(z) = \gamma_u^2 D_u/4N_u^2\, z$ [17]. This allows to extract them by fitting the intensity impulse responses of the individual mode groups at the output of the first fiber span with a Gaussian-shaped waveform with root-mean-square width equal to T_u.

We set $\alpha_a = \alpha_b = 0$ and $\vec{\alpha}_a = \vec{\alpha}_b = 0$ in the following discussion. We leave the analysis of MDL accumulation to Section IV-D.

The extraction of the inter-group coupling coefficients is more involved. Here we proceed by evaluating the evolution of the mean optical powers in the individual mode groups, as these quantities can be extracted from the experimental crosstalk matrix. To this end we make use of the Ito calculus [34], by first expressing (3) and (4) in the Stratonovich form, namely,

$$\mathrm{d}\vec{E}_a = i\omega\beta'_a\vec{E}_a\mathrm{d}z + i\omega\frac{\mathrm{d}\vec{W}_a\cdot\vec{\Lambda}_a}{2N_a}\vec{E}_a + i\mathrm{d}\mathbf{C}\vec{E}_b \tag{9}$$

$$\mathrm{d}\vec{E}_b = i\omega\beta'_b\vec{E}_b\mathrm{d}z + i\omega\frac{\mathrm{d}\vec{W}_b\cdot\vec{\Lambda}_b}{2N_b}\vec{E}_b + i\mathrm{d}\mathbf{C}^\dagger\vec{E}_a. \tag{10}$$

The Ito-corrected equations are obtained in the following form with the use of (5), (7) and (8),

$$\mathrm{d}\vec{E}_a = i\omega\beta'_a\vec{E}_a\mathrm{d}z + i\omega\frac{\mathrm{d}\vec{W}_a\cdot\vec{\Lambda}_a}{2N_a}\vec{E}_a + i\mathrm{d}\mathbf{C}\vec{E}_b - \omega^2\frac{\gamma_a^2 D_a}{8N_a^2}\vec{E}_a\mathrm{d}z - \frac{1}{2}\eta^2 2N_b\vec{E}_a\mathrm{d}z \tag{11}$$

$$\mathrm{d}\vec{E}_b = i\omega\beta'_b\vec{E}_b\mathrm{d}z + i\omega\frac{\mathrm{d}\vec{W}_b\cdot\vec{\Lambda}_b}{2N_b}\vec{E}_b + i\mathrm{d}\mathbf{C}^\dagger\vec{E}_a - \omega^2\frac{\gamma_b^2 D_b}{8N_b^2}\vec{E}_b\mathrm{d}z - \frac{1}{2}\eta^2 2N_a\vec{E}_b\mathrm{d}z. \tag{12}$$

The equations for the average powers carried by each mode group $I_a = \langle\vec{E}_a^\dagger\vec{E}_a\rangle$ and $I_b = \langle\vec{E}_b^\dagger\vec{E}_b\rangle$ are then obtained in the following form,

$$\mathrm{d}I_a = \eta^2 2N_a I_b\mathrm{d}z - \eta^2 2N_b I_a\mathrm{d}z \tag{13}$$

$$\mathrm{d}I_b = \eta^2 2N_b I_a\mathrm{d}z - \eta^2 2N_a I_b\mathrm{d}z, \tag{14}$$

or, equivalently,

$$\frac{\mathrm{d}}{\mathrm{d}z}\begin{bmatrix}I_a\\I_b\end{bmatrix} = \begin{bmatrix}-2\eta^2N_b & 2\eta^2N_a\\ 2\eta^2N_b & -2\eta^2N_a\end{bmatrix}\begin{bmatrix}I_a\\I_b\end{bmatrix} = \mathbf{K}\begin{bmatrix}I_a\\I_b\end{bmatrix}. \tag{15}$$

The solution to the above,

$$\begin{bmatrix}I_a(z)\\I_b(z)\end{bmatrix} = \exp(\mathbf{K}z)\begin{bmatrix}I_a(0)\\I_b(0)\end{bmatrix} = \mathbf{X}_g\begin{bmatrix}I_a(0)\\I_b(0)\end{bmatrix}, \tag{16}$$

can be mapped into experimental data, by establishing a relation between the matrix $\mathbf{X}_g$, which describes inter-mode-group crosstalk, and the experimentally measurable crosstalk matrix $\mathbf{X}$. This relation is not straightforward and is discussed in what follows. Prior to doing so, however, we note that the expression of $\mathbf{K}$ can be readily generalized to the case of more than two mode groups. For instance, in the case of three mode groups a, b, and c, it takes the following form

$$\begin{bmatrix}-2(\eta_{ab}^2N_b+\eta_{ac}^2N_c) & 2\eta_{ab}^2N_a & 2\eta_{ac}^2N_a\\ 2\eta_{ab}^2N_b & -2(\eta_{ab}^2N_a+\eta_{bc}^2N_c) & 2\eta_{bc}^2N_b\\ 2\eta_{ac}^2N_c & 2\eta_{bc}^2N_c & -2(\eta_{ac}^2N_a+\eta_{bc}^2N_b)\end{bmatrix} \tag{17}$$

where η_{uv}^2 is the coefficient that describes coupling between mode groups u and v. Fig. 8 illustrates the relation between $\mathbf{X}_g$, which is a $N_g\times N_g$ matrix (with N_g denoting the number of non-degenerate mode groups), and $\mathbf{X}$, which is an $N\times N$ matrix (with N denoting the total number of modes), in the case of a three-mode-group fiber. The figure relies on the fact that the simple model used in this work yields a crosstalk matrix $\mathbf{X}$ that is symmetric and made of blocks with identical elements[4] (the elements in each block are identical owing to the strong intra-group mixing). Therefore, each element in the mode-group

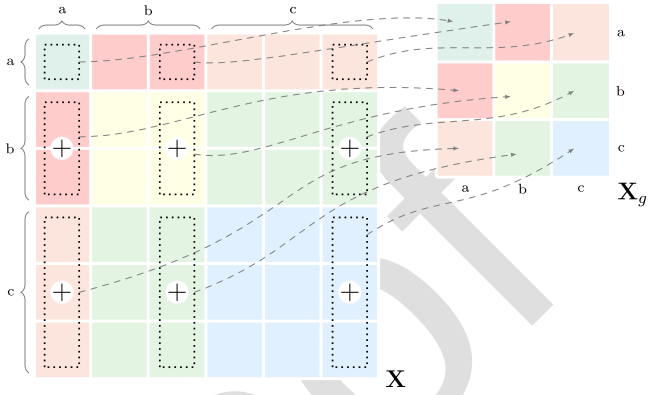

Fig. 8. Relation between the $N\times N$ crosstalk matrix $\mathbf{X}$ and the $N_g\times N_g$ matrix $\mathbf{X}_g$ describing inter-mode-group crosstalk, in the example of a three-mode-group fiber, where $N=6$ and $N_g=3$.

[4]Symmetry emerges immediately in the special case $N_a = N_b = N_c = 1$, where $\mathbf{X}$ and $\mathbf{X}_g$ coincide.

TABLE II
COUPLING COEFFICIENTS AT 1557.8 NM USED FOR SIMULATION

Coefficient	Value ($\mathrm{km}^{-1/2}$)	Coefficient	Value ($\mathrm{km}^{-1/2}$)
η_{ab}	0.0296	η_{bd}	0.0144
η_{ac}	0.0130	η_{be}	0.0129
η_{ad}	0.0297	η_{cd}	0.0150
η_{ae}	0.0129	η_{ce}	0.0302
η_{bc}	0.0147	η_{de}	0.0325

crosstalk matrix $\mathbf{X}_g$ corresponding to a specific pair of mode groups is obtained by summing the elements of any one column of $\mathbf{X}$ that also corresponds to the same pair of mode groups. For instance, the (b, c) element of $\mathbf{X}_g$ can be obtained by summing the second and third elements of the sixth column of $\mathbf{X}$ (or, equivalently, the second and third elements of the fourth or the fifth column of $\mathbf{X}$). Note that all the elements in each column (or row) of $\mathbf{X}$ sum to unity, as a result of unitary propagation assumed in the model.

Extracting the 5×5 matrix $\mathbf{X}_g$ from the experimental 15×15 crosstalk matrix $\mathbf{X}_{\text{exp}}$ is not as straightforward, as in practice $\mathbf{X}_{\text{exp}}$ never takes the highly symmetric form illustrated in Fig. 8. Note that by $\mathbf{X}_{\text{exp}}$ we denote the time- and polarization-averaged absolute square fiber impulse response matrix, measured for a single MMF span. The first step towards extracting the ten coupling coefficients (one per each pair of mode groups) is therefore enforcing this form into $\mathbf{X}_{\text{exp}}$, which is done as follows. The matrix $\mathbf{X}_{\text{exp}}$ is first normalized so that the sum of each column's elements equals one. The obtained matrix (that in practice is slightly asymmetric) is then symmetrized into $\tilde{\mathbf{X}}_{\text{exp}} = (\mathbf{X}_{\text{exp}} + \mathbf{X}_{\text{exp}}^t)/2$. To shape $\tilde{\mathbf{X}}_{\text{exp}}$ into the form depicted in Fig. 8, all the elements within each of the off-diagonal blocks are replaced with their respective averages. Subsequently, normalization of each column is re-enforced by setting the elements in each diagonal square box with identical values so that the sum of the elements in each column equals one. The resulting matrix can then be used to extract $\mathbf{X}_g$ as illustrated in Fig. 8, and the ten coupling coefficients are obtained from the off-diagonal elements of $\log(\mathbf{X}_g)/L_s$, where L_s is the span length.

B. Numerical Simulation

In the numerical simulation, propagation is modeled based on (3) and (4), generalized for five mode groups. A 15-mode fiber span of length $L_s = 58.9$ km (consistent with the experiment) is emulated. It is implemented as a concatenation of $\mathcal{N} = 400$ wave-plates of width $\Delta z = L_s/\mathcal{N}$. The transfer matrix of each wave-plate $\mathbf{U}_{\text{wp}}$ is then characterized by $\exp(i\mathbf{M}\Delta z)$, with

$$\mathbf{M} = \begin{bmatrix} \frac{\vec{W}_a \cdot \vec{\Lambda}_a}{2N_a}\omega & \mathbf{C}_{ab} & \mathbf{C}_{ac} & \mathbf{C}_{ad} & \mathbf{C}_{ae} \\ \mathbf{C}_{ab}^\dagger & \frac{\vec{W}_b \cdot \vec{\Lambda}_b}{2N_b}\omega & \mathbf{C}_{bc} & \mathbf{C}_{bd} & \mathbf{C}_{be} \\ \mathbf{C}_{ac}^\dagger & \mathbf{C}_{bc}^\dagger & \frac{\vec{W}_c \cdot \vec{\Lambda}_c}{2N_c}\omega & \mathbf{C}_{cd} & \mathbf{C}_{ce} \\ \mathbf{C}_{ad}^\dagger & \mathbf{C}_{bd}^\dagger & \mathbf{C}_{cd}^\dagger & \frac{\vec{W}_d \cdot \vec{\Lambda}_d}{2N_d}\omega & \mathbf{C}_{de} \\ \mathbf{C}_{ae}^\dagger & \mathbf{C}_{be}^\dagger & \mathbf{C}_{ce}^\dagger & \mathbf{C}_{de}^\dagger & \frac{\vec{W}_e \cdot \vec{\Lambda}_e}{2N_e}\omega \end{bmatrix}. \tag{18}$$

As discussed in the previous section, the terms in the main diagonal describe intra-group mode dispersion. The vectors $\vec{W}_u$ $(u \in \{a, b, c, d, e\})$ are all independently generated and their components are independent Gaussian random variables with zero mean and standard deviation equal to $\gamma_u/\sqrt{\Delta z}$, consistent with (5). The matrix $\mathbf{C}_{uv}$ $(u, v \in \{a, b, c, d, e\})$ describes coupling between mode groups u and v. The coupling matrices are generated independently of one another and, in accordance with (7) and (8), their elements are independent complex-valued Gaussian random variables with zero mean, uncorrelated real and imaginary parts, and standard deviation equal to $\eta_{uv}/\sqrt{\Delta z}$.

Consistently with the experimental settings, the fiber-span transfer matrix $\mathbf{T}_s(\omega)$ is calculated in a frequency band of 24.5 GHz. Multiple recirculations are described in the frequency domain by the matrix $\mathbf{T}_s(\omega)\mathbf{P}\mathbf{T}_s(\omega)\cdots\mathbf{P}\mathbf{T}_s(\omega)$, where by $\mathbf{P}$ we denote a 30×30 matrix that implements ideal MP. The inverse Fourier transform of the accumulating matrix is used to evaluate the intensity impulse response at every recirculation. The parameters used in the simulations for the wavelength channel at 1557.8 nm are listed in Tables I and II.

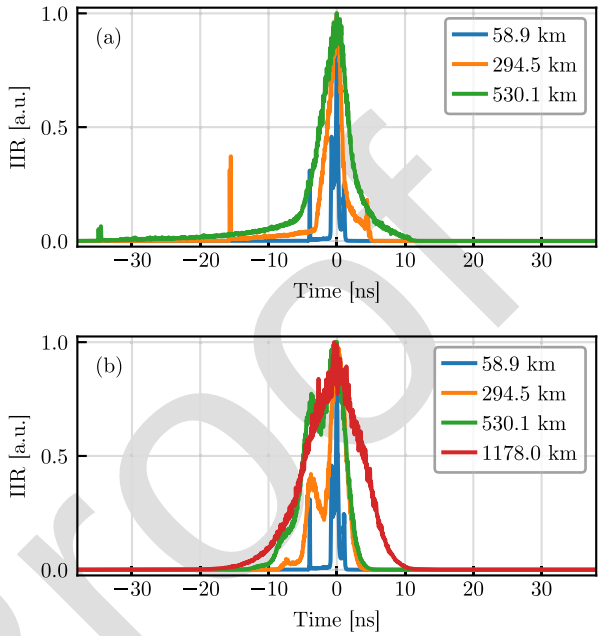

Fig. 9. Simulated IIR for various transmission distances at 1557.8 nm (a) in the absence of MP and (b) with NC-MGP.

C. Simulation Results: Modal Dispersion

Fig. 9 shows a plot of the simulated IIR of the wavelength channel at 1557.8 nm, for the same propagation distances and MP settings as in Fig. 4. A qualitative similarity between the two figures can be noticed.

Fig. 10(a) shows the plot of the IIR duration versus propagation distance for the same wavelength channel (the duration of the simulated IIR is calculated to be the period of time which encompasses 98% of the IIR energy, as in the experiment). Similarly, Fig. 10(b) illustrates the extension of the same analysis to all five channels, with their average IIR duration plotted versus propagation distance. In both figures, a square-root fit is also plotted for comparison. The plot indicates that, on average, all

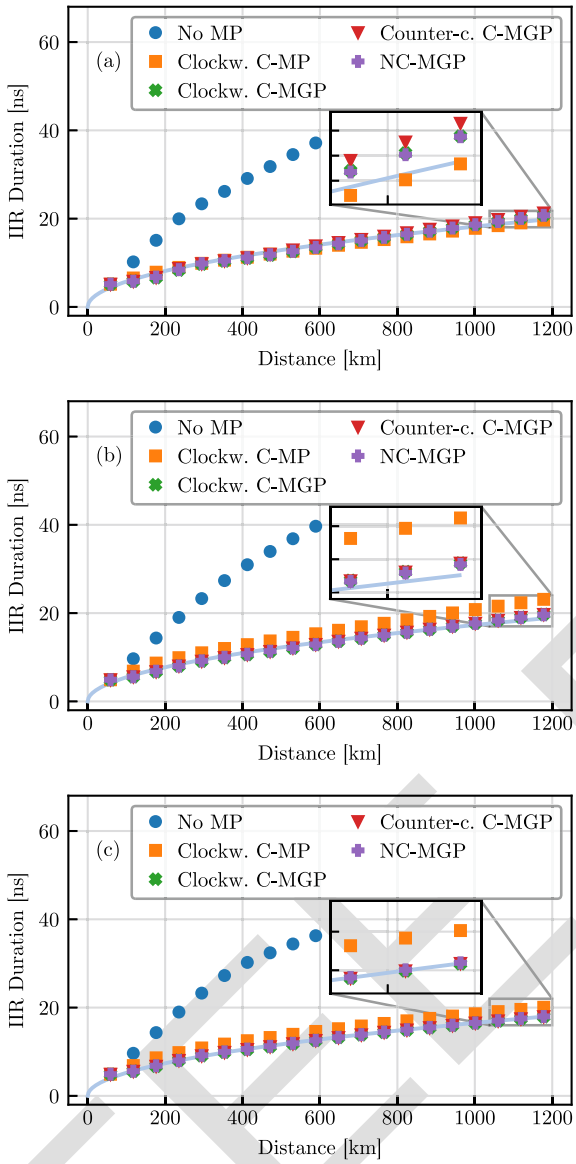

Fig. 10. (a) Simulated-IIR duration of the wavelength channel at 1557.8 nm versus propagation distance in the recirculating-loop configuration. (b) Simulated-IIR duration averaged over the five wavelength channels used in the experiment versus propagation distance in the recirculating-loop configuration. (c) Same as in (b) for a link with independent fiber spans. The line spacings in the insets of (b) and (c) are 2 ns.

permutation schemes yield similar results in remarkable agreement with the experiment, with the C-MP scheme, performing slightly lower than the others. Specifically, at 1178 km, it results in an IIR duration approximately 2 ns greater than for the other schemes. This suggests that in the propagation regime of our experiment, inter-group coupling is more critical than delay management in implementing MP. The fact that no difference in performance between the C-MP scheme and the other schemes is observed experimentally, must be ascribed to additional coupling introduced in the experimental setup. Indeed, in our model we assume that coupling occurs only during fiber propagation, whereas multiplexing, de-multiplexing and MP are implemented ideally, that is by introducing no additional cross-talk.

We used the model developed for propagation in the 15-mode fiber, to evaluate the performance of the permutation schemes in a realistic multi-span fiber system, where permutation is performed between independent fiber spans. To this end, we simulated a fiber link composed of 20 fiber spans, where each span was generated independently as described above. Fig. 10(c) illustrates the IIR duration evaluated at the end of each span for all permutation schemes. Note that, similar to Fig. 10(b), each data point in the figure is obtained by averaging the IIR duration of the MMF link across the five wavelength channels spanning the C-band. Compared to the recirculating-loop configuration, only a small additional reduction in the IIR duration is observed, which further supports the reliability of our experimental findings in predicting the performance of MP in field-deployed multi-span fiber links.

It is worth stressing that the effectiveness of the C-MP scheme is strongly influenced by the fact that the fastest mode (LP_{01}) is always mapped into the slowest mode group (LP_{11}). This suggests a dependence on the details of the MMF design for this scheme's performance. Indeed, we verified through simulations that exchanging the group velocities of the five mode groups may substantially deteriorate the performance of the C-MP scheme, while having negligible practical impact on the performance of the other schemes.

D. Simulation Results: Mode-Dependent Loss

As observed in Section III-B2, MDL accumulates with propagation distance in the same way with and without MP. A possible explanation for this evidence is that MDL accumulates within groups of strongly coupled modes as a result of random and distributed local MDL, compatible with multiple fiber splices, thereby growing proportionally to the square root of propagation distance even in the absence of MP. Independence of the MDL accumulation on the mode permutation scheme has also been reported in [30], where it was argued that this might follows from the fact that MDL is mainly introduced by the single-mode stages connecting two recirculating loops.

To assess which one of the two assumptions is consistent with the experimental observations, we describe the accumulation of distributed MDL at the center frequency by simply setting $\omega = 0$ in (3) and (4). Conversely, we account for the case of MDL introduced by the single-mode stage by adding independent gain fluctuations with a Gaussian distribution and suitable strength to the propagating space and polarization modes between two recirculations, while assuming that the multimode fiber itself is unitary, that is, assuming $\alpha_a = \alpha_b = 0$ in (3) and (4). In both cases, a random phase is applied to each space and polarization mode between two recirculations, in order to account for the effect of the AOMs that are used in the loop as optical switches (the AOMs apply an 80 MHz frequency shift when they route the impinging signal towards the next circulation). Note that while the local MDL and the gain fluctuations are *frozen* from recirculation to recirculation, the random phases change from recirculation to recirculation as a result of the linewidth (resulting from frequency fluctuations) of the modulation applied by the AOMs. It is worth noting that the AOMs play an important

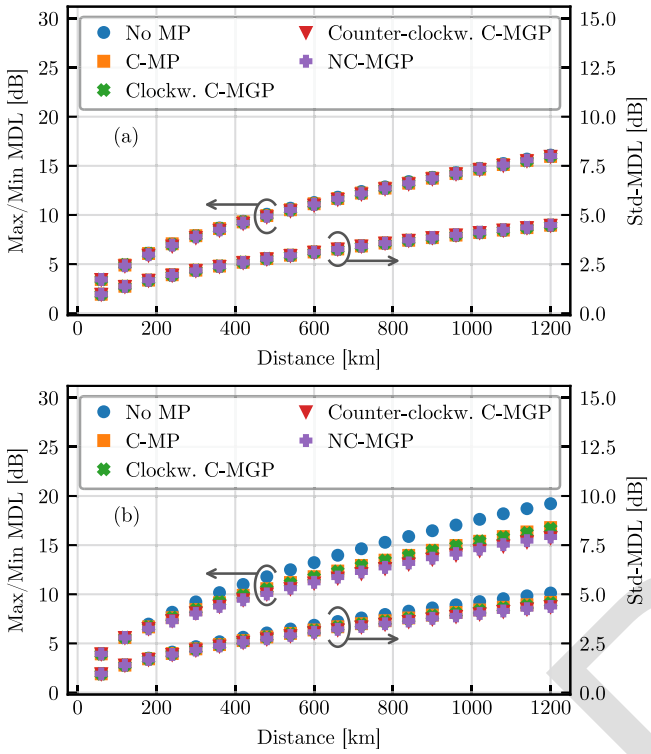

Fig. 11. Simulated Max/Min MDL and Std-MDL for the wavelength channel at 1557.8 nm versus propagation distance in the recirculating-loop configuration assuming (a) Distributed MDL, and (b) Single-mode gain fluctuations.

role in shaping the growth of MDL with propagation distance. In fact, this approaches a quasi-linear accumulation if no phase fluctuation is introduced, as is the case when electro-optic modulators are used as optical switches [35].

The simulation results are shown in Fig. 11, where we plot the average MDL versus propagation distance in the absence of mode permutation and for the considered MP schemes. The averaging is performed over 1000 link transfer matrices obtained for as many independent instantiations of the random quantities involved. Fig. 11(a) refers to the case of distributed MDL, and Fig. 11(b) to the case of single-mode gain fluctuations. Intra-group coupling was introduced so as to enforce a decorretalation length of 1km in each mode group [33]. For the inter-mode group coupling we assumed the coefficient values in Table II. For the local MDL strength, which is characterized by the coefficients ζ_u defined through (6), we assumed one of the many sets of numerical values that are compatible with an accumulated mean MDL of approximately 15 dB after 1200 km, as observed in the experiment. Finally, for the gain fluctuations, based on the same criterion, we assumed a standard deviation of 0.5 dB.

Inspection of Fig. 11 suggests that while MDL accumulation is similar across all considered schemes in both models, the model based on distributed MDL is more consistent with the experimental finding. Therefore, we conclude that distributed random MDL, possibly arising from fiber splices (seven in the experiment, one every less than 8 km in the loop), may be the predominant (yet not the only one) mechanism contributing to MDL accumulation in MMF links.

V. Conclusion

We experimentally investigated the effectiveness of four mode-permutation schemes in reducing the accumulation of modal dispersion in a long-haul 15-mode fiber link. We found that with mode permutation, the duration of the intensity impulse response of the MMF link increased proportionally to the square root of transmission distance, rather than linearly with it, as is the case in the absence of mode permutation. This reduced considerably the complexity of the receiver MIMO-DSP. We estimated an extension of the system reach from 530 km to 1178 km, enabled by a reduction in the time-domain equalizer window from 71.4 ns to 38.8 ns. Although no transmission results are shown in this work, such an extension has been demonstrated with a full C-band transmission in ref. [25]. The considered permutation schemes exhibited comparable performance with little wavelength dependence across the C-band. We also developed a simple model to simulate propagation in multi-mode fibers, whose parameters can be conveniently extracted from the experimental data. Simulations indicate negligible difference between the experimental results obtained in a recirculating-loop configuration and the performance of mode permutation in a realistic fiber link composed of independent fiber spans.

References

[1] P. J. Winzer and D. T. Neilson, "From scaling disparities to integrated parallelism: A decathlon for a decade," *J. Lightw. Technol.*, vol. 35, no. 5, pp. 1099–1115, Mar. 2017.

[2] A. Chraplyvy, "Plenary paper: The coming capacity crunch," in *Proc. IEEE 35th Eur. Conf. Opt. Commun.*, 2009, p. 1.

[3] B. J. Puttnam, G. Rademacher, and R. S. Luís, "Space-division multiplexing for optical fiber communications," *Optica*, vol. 8, no. 9, pp. 1186–1203, 2021. [Online]. Available: https://opg.optica.org/optica/abstract.cfm?URI=optica-8-9-1186

[4] S. Matsuo et al., "High-spatial-Multiplicity multicore fibers for future dense space-division-multiplexing systems," *J. Lightw. Technol.*, vol. 34, no. 6, pp. 1464–1475, Mar. 2016.

[5] R. Ryf et al., "Mode-division multiplexing over 96 km of few-mode fiber using coherent 6 MIMO processing," *J. Lightw. Technol.*, vol. 30, no. 4, pp. 521–531, Feb. 2012.

[6] N. K. Fontaine et al., "3030 MIMO transmission over 15 spatial modes," presented at Opt. Fiber Commun. Conf. Post Deadline Papers, Los Angeles, CA, USA, Mar. 22–26, 2015, Paper Th5C.1. [Online]. Available: https://opg.optica.org/abstract.cfm?URI=OFC-2015-Th5C.1

[7] G. Rademacher et al., "Peta-bit-per-second optical communications system using a standard cladding diameter 15-mode fiber," *Nature Commun.*, vol. 12, no. 1, 2021, Art. no. 4238, doi: 10.1038/s41467-021-24409-w.

[8] G. Rademacher et al., "1.53 peta-bit/s C-band transmission in a 55-Mode fiber," in *Proc. Eur. Conf. Opt. Commun.*, 2022, pp. 1–4. [Online]. Available: https://opg.optica.org/abstract.cfm?URI=ECEOC-2022-Th3C.3

[9] K. Shibahara et al., "DMD-Unmanaged long-haul SDM transmission over 2500-km 12-Core 3-Mode MC-FMF and 6300-km 3-mode FMF employing intermodal interference canceling technique," *J. Lightw. Technol.*, vol. 37, no. 1, pp. 138–147, Jan. 2019. [Online]. Available: https://opg.optica.org/jlt/abstract.cfm?URI=jlt-37-1-138

[10] K. Shibahara et al., "Long-haul DMD-Unmanaged 6-Mode-Multiplexed transmission employing cyclic mode-group permutation," in *Proc. IEEE Opt. Fiber Commun. Conf.*, 2020, pp. 1–3. [Online]. Available: https://opg.optica.org/abstract.cfm?URI=OFC-2020-Th3H.3

[11] K. Shibahara, M. Hoshi, and Y. Miyamoto, "10-spatial-mode 1300-km transmission over 6-LP graded index few-mode fiber with 36-ns modal dispersion," presented at Proc. Opt. Fiber Commun. Conf., San Diego, CA, USA, Mar. 5–9, 2023, p. M2B.2. [Online]. Available: https://opg.optica.org/abstract.cfm?URI=OFC-2023-M2B.2

[12] M. v. d. Hout et al., "273.6 Tb/s transmission over 1001 km of 15-Mode fiber using 16-QAM C-band signals," in *2023 Opt. Fiber Commun. Conf. Exhib.*, 2023, pp. 1–3.

[13] G. D. Sciullo et al., "Modal dispersion mitigation in a long-haul 15-Mode fiber link through mode permutation," in *2023 IEEE Photon. Soc. Summer Topicals Meeting Ser.*, 2023, pp. 1–2.
[14] X. Liu, Y. Wang, Q. Huang, and D. Zhang, "A joint mode permutation architecture for 10-Mode-Multiplexed long-haul transmissions," in *2024 Opt. Fiber Commun. Conf. Exhib.*, 2024, pp. 1–3.
[15] Y. Wang, X. Liu, Q. Huang, and D. Zhang, "10-mode PM-QPSK transmission over 2320 km enabled by optimized mode permutation strategies," presented at Opt. Fiber Commun. Conf. Exhib., San Diego, CA, USA, Mar. 24–28, 2024, Paper Th1H.7.
[16] C. Antonelli, A. Mecozzi, M. Shtaif, and P. J. Winzer, "Stokes-space analysis of modal dispersion in fibers with multiple mode transmission," *Opt. Exp.*, vol. 20, no. 11, pp. 11718–11733, 2012. [Online]. Available: https://opg.optica.org/oe/abstract.cfm?URI=oe-20-11-11718
[17] A. Mecozzi, C. Antonelli, and M. Shtaif, "Intensity impulse response of SDM links," *Opt. Exp.*, vol. 23, no. 5, pp. 5738–5743, 2015. [Online]. Available: http://www.osapublishing.org/oe/abstract.cfm?URI=oe-23-5-5738
[18] S. O. Arik, K.-P. Ho, and J. M. Kahn, "Group delay management and multiinput multioutput signal processing in mode-division multiplexing systems," *J. Lightw. Technol.*, vol. 34, no. 11, pp. 2867–2880, Jun. 2016. [Online]. Available: https://opg.optica.org/jlt/abstract.cfm?URI=jlt-34-11-2867
[19] G. Di Sciullo et al., "Reduction of modal dispersion in a long-haul 15-mode fiber link by means of mode permutation," in *Proc. 49th Eur. Conf. Opt. Commun.*, 2023, vol. 2023, pp. 250–253.
[20] A. Gatto et al., "Partial MIMO-based mode division multiplexing transmission over the first field-deployed 15-Mode fiber in metro scenario," in *2023 Opt. Fiber Commun. Conf. Exhib.*, 2023, pp. 1–3.
[21] P. Parolari et al., "Demonstration of multi-hop mode-group routing in a field-deployed multi-mode fiber network," in *2023 Opt. Fiber Commun. Conf. Exhib.*, 2023, pp. 1–3.
[22] N. K. Fontaine et al., "Broadband 15-Mode multiplexers based on multi-plane light conversion with 8 planes in unwrapped phase space," presented at Proc. Eur. Conf. Opt. Commun., Basel, Switzerland, Sep. 18–22, 2022, Paper We3A.2. [Online]. Available: https://opg.optica.org/abstract.cfm?URI=ECEOC-2022-We3A.2
[23] P. Sillard et al., "Low-differential-mode-group-delay 9-LP-mode fiber," *J. Lightw. Technol.*, vol. 34, no. 2, pp. 425–430, Jan. 2016.
[24] R. Ryf et al., "Space-division multiplexed transmission over 4200-km 3-Core microstructured fiber," presented at Proc. Nat. Fiber Optic Eng. Conf., Los Angeles, CA, USA, 2012, Paper PDP5C.2. [Online]. Available: https://opg.optica.org/abstract.cfm?URI=NFOEC-2012-PDP5C.2
[25] M. van den Hout et al., "Transmission of 273.6 Tb/s over 1001 km of 15-Mode multi-mode fiber using C-band only 16-QAM signals," *J. Lightw. Technol.*, vol. 42, no. 3, pp. 1136–1142, Feb. 2024. [Online]. Available: https://opg.optica.org/jlt/abstract.cfm?URI=jlt-42-3-1136
[26] P. J. Winzer and G. J. Foschini, "MIMO capacities and outage probabilities in spatially multiplexed optical transport systems," *Opt. Exp.*, vol. 19, no. 17, pp. 16680–16696, 2011. [Online]. Available: https://opg.optica.org/oe/abstract.cfm?URI=oe-19-17-16680
[27] K.-P. Ho and J. M. Kahn, "Mode-dependent loss and gain: Statistics and effect on mode-division multiplexing," *Opt. Exp.*, vol. 19, no. 17, pp. 16612–16635, 2011. [Online]. Available: https://opg.optica.org/oe/abstract.cfm?URI=oe-19-17-16612
[28] A. Andrusier, M. Shtaif, C. Antonelli, and A. Mecozzi, "Assessing the effects of mode-dependent loss in space-division multiplexed systems," *J. Lightw. Technol.*, vol. 32, no. 7, pp. 1317–1322, Apr. 2014.
[29] C. Antonelli, A. Mecozzi, M. Shtaif, and P. J. Winzer, "Modeling and performance metrics of MIMO-SDM systems with different amplification schemes in the presence of mode-dependent loss," *Opt. Exp.*, vol. 23, no. 3, pp. 2203–2219, 2015. [Online]. Available: https://opg.optica.org/oe/abstract.cfm?URI=oe-23-3-2203
[30] K. Shibahara et al., "Full C-band 3060-km DMD-Unmanaged 3-Mode transmission with 40.2-Tb/s capacity using cyclic mode permutation," *J. Lightw. Technol.*, vol. 38, no. 2, pp. 514–521, Jan. 2020.
[31] L. Dallachiesa et al., "Mode-group-Division multiplexing over a deployed 15-Mode-Fiber cable," in *2023 Opt. Fiber Commun. Conf. Exhib.*, 2023, pp. 1–3.
[32] G. Rademacher et al., "Characterization of the first field-deployed 15-Mode fiber cable for high density space-division multiplexing," presented at Proc. Eur. Conf. Opt. Commun., Basel, Switzerland, Sep. 18–22, 2022, Paper Th3B.1. [Online]. Available: https://opg.optica.org/abstract.cfm?URI=ECEOC-2022-Th3B.1
[33] G. Rademacher et al., "Random coupling between groups of degenerate fiber modes in mode multiplexed transmission," *Opt. Exp.*, vol. 21, no. 8, pp. 9484–9490, 2013. [Online]. Available: https://opg.optica.org/oe/abstract.cfm?URI=oe-21-8-9484
[34] C. W. Gardiner, *Stochastic Methods for Physics, Chemistry and Natural Sciences*. New York, NY, USA: Springer-Verlag, 1983.
[35] R. Ryf et al., "Transmission over randomly-coupled 4-core fiber in field-deployed multi-core fiber cable," in *2020 Eur. Conf. Opt. Commun.*, 2020, pp. 1–4.

Enhancing Long-Haul 15-Mode Fiber Performance: Mode Permutation for Reduced Modal Dispersion

Giammarco Di Sciullo, *Graduate Student Member, IEEE*, Divya A. Shaji, *Graduate Student Member, IEEE*, Menno van den Hout, *Student Member, IEEE*, Georg Rademacher, *Senior Member, IEEE*, Ruben S. Luís, *Senior Member, IEEE*, Benjamin J. Puttnam, *Member, IEEE*, Nicolas K. Fontaine, *Fellow, IEEE, Fellow, Optica*, Roland Ryf, *Fellow, IEEE, Fellow, Optica*, Haoshuo Chen, Mikael Mazur, *Member, IEEE*, David T. Neilson, *Fellow, IEEE*, Pierre Sillard, *Member, IEEE*, Frank Achten, Jun Sakaguchi, *Member, IEEE*, Chigo Okonkwo, *Senior Member, IEEE*, Antonio Mecozzi, *Fellow, IEEE, Fellow, Optica*, Cristian Antonelli, *Senior Member, IEEE, Senior Member, Optica*, and Hideaki Furukawa, *Member, IEEE*

***Abstract*—We explore the efficacy of mode permutation to mitigate the impact of modal dispersion in a 15-mode fiber link for long-haul space-division multiplexed transmission. By introducing strong coupling between all the fiber modes, mode permutation reduces the growth rate of the link's intensity impulse response (IIR) with transmission distance, yielding a reduction in the receiver MIMO-DSP complexity. Using a recirculating fiber-loop configuration, we experimentally compare four permutation schemes and find that they are similarly effective in reducing the increase of the IIR duration from proportional to the square-root of propagation distance. At the reach of 530 km – the largest achievable with the time-domain MIMO window of 71.4 ns available in the experiment in the absence of mode permutation – the IIR duration is seen to reduce from almost 40 ns to less than 15 ns, while the maximum reach achieved with the use of mode permutation increases to 1178 km. We also devise a simple model to simulate propagation in realistic MMF links with independent fiber spans, whose parameters can be conveniently extracted from the data. In achieving good agreement between the simulated and experimental results, the model suggests that the effectiveness of mode permutation in a realistic 15-mode fiber link, composed of independent fiber spans, is only slightly greater than in the experimental recirculating-loop configuration.**

***Index Terms*—Modal dispersion, multi-mode fiber transmission, mode permutation, space-division multiplexing.**

Received 12 April 2024; revised 29 July 2024 and 27 August 2024; accepted 30 August 2024. This work was supported in part by Italian Government through INCIPICT and FIRST Projects and in part by KPN-TU/e Smart Two Program and European Union's Horizon Europe Research and Innovation Programme under the Marie Sklodowska- Curie Grant Agreement Number 101072409. *(Corresponding author: Giammarco Di Sciullo.)*

Giammarco Di Sciullo is with the Photonic Network System Laboratory, National Institute of Information and Communications Technology, Tokyo 184-8795, Japan, and also with the University of L'Aquila and CNIT, 67100 L'Aquila, Italy (e-mail: giammarco.disciullo@graduate.univaq.it).

Divya A. Shaji, Antonio Mecozzi, and Cristian Antonelli are with the University of L'Aquila and CNIT, 67100 L'Aquila, Italy (e-mail: divyaann.shaji@univaq.it; antonio.mecozzi@univaq.it; cristian.antonelli@univaq.it).

Menno van den Hout is with the Photonic Network System Laboratory, National Institute of Information and Communications Technology, Tokyo 184-8795, Japan, and also with the High Capacity Optical Transmission Laboratory, Electro-Optical Communications Group, Eindhoven University of Technology, 5600MB Eindhoven, The Netherlands (e-mail: m.v.d.hout@tue.nl).

Georg Rademacher is with the Photonic Network System Laboratory, National Institute of Information, and Communications Technology, Tokyo 184-8795, Japan. He is now with the Institute of Electrical and Optical Communications, University of Stuttgart, 70174 Stuttgart, Germany (e-mail: georg.rademacher@int.uni-stuttgart.de).

Ruben S. Luís, Benjamin J. Puttnam, Jun Sakaguchi, and Hideaki Furukawa are with the Photonic Network System Laboratory, National Institute of Information and Communications Technology, Tokyo 184-8795, Japan (e-mail: rluis@nict.go.jp; ben@nict.go.jp; jsakaguchi@nict.go.jp; furukawa@nict.go.jp).

Nicolas K. Fontaine, Roland Ryf, Haoshuo Chen, Mikael Mazur, and David T. Neilson are with Nokia Bell Labs, New Providence, NJ 07974 USA (e-mail: nicolas.fontaine@nokia-bell-labs.com; roland.ryf@nokia-bell-labs.com; haoshuo.chen@nokia-bell-labs.com; mikael.mazur@nokia-bell-labs.com; david.neilson@nokia-bell-labs.com).

Pierre Sillard is with Prysmian Group, 62092 Haisnes Cedex, France (e-mail: pierre.sillard@prysmiangroup.com).

Frank Achten is with Prysmian Group, 5651 CA Eindhoven, The Netherlands (e-mail: frank.achten@prysmiangroup.com).

Chigo Okonkwo is with the High Capacity Optical Transmission Laboratory, Electro-Optical Communications Group, Eindhoven University of Technology, 5600MB Eindhoven, The Netherlands (e-mail: c.m.okonkwo@tue.nl).

Color versions of one or more figures in this article are available at https://doi.org/10.1109/JLT.2024.3453553.

Digital Object Identifier 10.1109/JLT.2024.3453553

I. Introduction

As DEMAND for higher data rates is expected to continue its exponential increase in optical fiber networks, and single-mode optical fibers are reaching their transmission limits [1], space-division multiplexing (SDM) has gained traction as a promising alternative to address the impending capacity crunch [2]. Proposed SDM fibers include multi-core fibers (MCFs), multi-mode fibers (MMFs) and hybrid multi-core multi-mode fibers (MC-MMFs) [3]. Specifically, MMFs, wherein discrete data signals are multiplexed across distinct spatial modes can support a substantial quantity of spatial channels within the same 125 μm cladding diameter as standard single-mode fibers (SMFs). This characteristic ensures similar fiber mechanical reliability and compatibility with current cabling and manufacturing processes [4]. Nonetheless, the accumulation of modal dispersion (MD) has a direct impact on the required memory length for the multiple-input multiple-output (MIMO) equalizer [5], imposing constraints on both mode count and transmission reach. Indeed, while short-distance transmission utilizing MMFs with up to 55 modes has been recently reported [6],

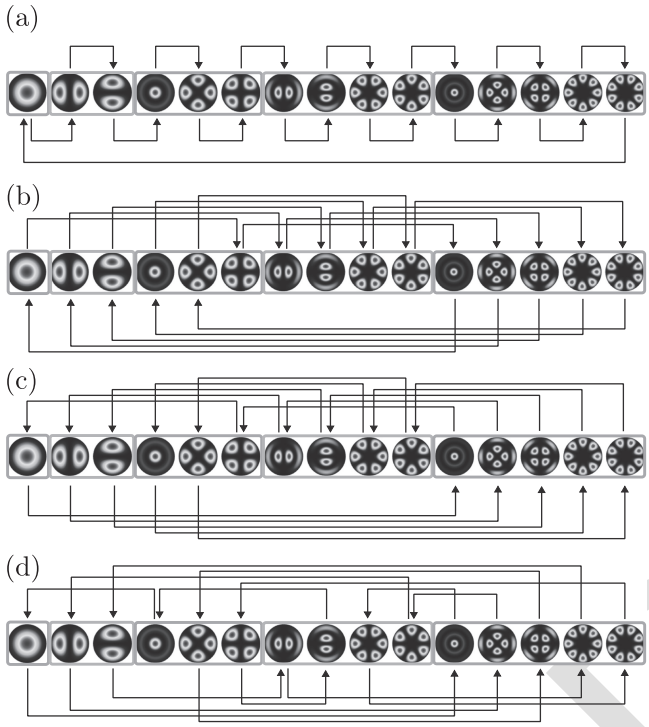

Fig. 1. Sketch of the considered mode permutation schemes: (a) C-MP, (b) Clockwise C-MGP, (c) Counter-clockwise C-MGP and (d) NC-MGP.

[7], [8], experiments targeting long-haul transmission have only used up to 15 fiber modes [9], [10], [11], [12], [13], [14], [15]. In addressing the accumulation of MD, a strategic approach involves intentionally inducing strong mode coupling within the MMF link. This method is grounded in the understanding that modal dispersion increases proportionally to the square root of the propagation distance under conditions of strong mode mixing, as opposed to a proportional increase with propagation distance in situations marked by no-to-weak mode coupling [16], [17], [18]. In pursuit of robust mode coupling to counteract the accumulation of MD, a practical implementation involves the incorporation of lumped mode scramblers along the fiber link. This method stands as a viable scheme, strategically implemented to enhance mode mixing and mitigate MD effects, offering a solution to optimize the performance of the MMF link [18]. It is scalable for arbitrary mode counts, thereby providing a practical approach for future MMF system deployments. Recent advancements in this scheme include the proposals of cyclic mode permutation (C-MP) and cyclic mode-group permutation (C-MGP), demonstrating evolving techniques to further refine and improve the effectiveness of the mode coupling strategy [9], [10], [11], [12], [13].

In this work we examine the efficacy of four distinct mode permutation (MP) schemes within a recirculating-loop-based, long-haul 15-mode fiber link, expanding on [19]. Employing these permutation schemes allowed extending the transmission reach from 530 km to 1178 km while significantly reducing the complexity of the receiver MIMO digital signal processing (DSP). Notably, at 530 km, there was a reduction exceeding 65% in the duration of the MMF link intensity impulse response (IIR). An important supplement to the original work in [19] is the study of mode-dependent loss (MDL) in the MMF system, which shows that MP does not affect MDL accumulation with transmission distance. We also developed a simple model for the simulation of multi-mode propagation to assess the effectiveness of MP in realistic links with independent fiber spans, as opposed to the recirculating-loop scheme used in the experiment. The model relies on a handful of parameters that can be conveniently extracted from the experimental data. Despite its simplicity, the model demonstrated accuracy in reproducing the experimental results. Numerical results obtained for a link composed of independent fiber spans showed only a modest improvement in the performance of MP compared to the recirculating-loop configuration, further supporting the reliability and applicability of the experimental findings. Finally, the model was used to explain the observed independence of MDL accumulation on MP.

The remainder of this paper is organized as follows. Section II delves into the concept of mode permutation and introduces the schemes examined in the experiment. Section III outlines the experimental setup and presents the obtained results. In Section IV, a simulation framework complementing the experimental results is introduced and the corresponding findings are presented. The conclusions of this work are drawn in Section V.

II. Mode Permutation Schemes

Graded-index-core multi-mode fibers are characterized by the existence of non-degenerate mode groups, such that modes within the same group couple strongly during propagation, whereas modes belonging to different groups are weakly coupled and the extent to which they mix increases with propagation distance. In short-reach applications, where the inter-mode-group coupling is negligible, the individual mode groups can be addressed independently with a considerable simplification of the receiver MIMO [20], [21]. However, in metro-to-long-haul applications that are of interest for this work, a full-MIMO approach (where all the fiber modes are processed jointly) becomes necessary, in spite of the fact that non-degenerate mode groups may remain only partially coupled. In this regime MD, which is typically quantified in terms of the link's IIR duration, increases linearly with propagation distance at first, transiting to some sub-linear growth when inter-mode-group coupling becomes substantial. The complexity of the receiver MIMO-DSP grows accordingly. In this scenario, strong coupling between all modes is preferred. In fact, in the regime of strong mode mixing, MD is known to grow only proportionally to the square root of propagation distance [16], [17], [18], implying a drastic reduction in the MIMO-DSP complexity compared to the regime of partial mode coupling.

A practical approach to induce strong coupling between modes belonging to different groups involves the introduction of lumped mode scramblers along the MMF link. In this study, we investigate the effectiveness of four distinct MP schemes in introducing strong mode mixing along a multi-span MMF link, where MP is implemented through a de-multiplexer/multiplexer (De-MUX/MUX) device pair at the end of each span. The first

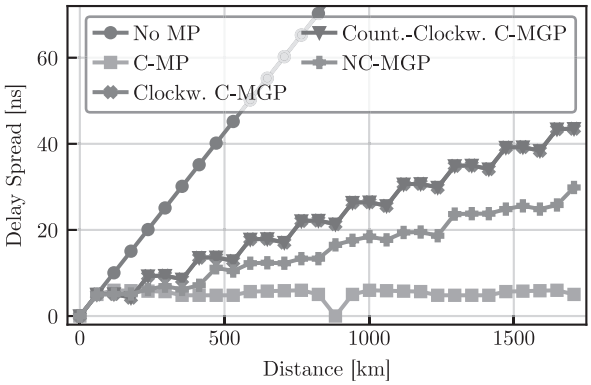

Fig. 2. Delay spread versus propagation distance in the absence of mode coupling in the MMF spans, with and without MP, as obtained through numerical simulation.

device serves to separate the multi-mode field at the output of the MMF into individual single-mode fields. These are subsequently cross-connected to the single-mode sections of the recirculating loop, which guide the signal back to the input of the second device. Fig. 1 illustrates the mode permutation schemes under consideration for the 15-mode fiber used in the experiment. The first scheme [9] (Fig. 1(a)), employs unitary C-MP. In this method, the 15 spatial modes undergo a cyclic shift, moving one position towards higher-order modes at each permutation stage. The second [12], [13] and third schemes, involve the cyclic clockwise (clockwise C-MGP, Fig. 1(b)) and counter-clockwise (counter-clockwise C-MGP, Fig. 1(c)) shifts of the 15 spatial modes by five positions, corresponding to the largest mode-group size. These schemes exhibit a periodic pattern, where spatial modes revert to their initial configuration after either 15 or 3 permutation stages, respectively. Introducing a novel approach in our work [19], the fourth scheme (Fig. 1(d)), referred to as non-cyclic mode-group permutation (NC-MGP), breaks away from periodicity by implementing controlled inter-mode-group permutation. In this scheme, spatial modes within a given mode group are mapped onto other spatial modes of the remaining mode groups, with careful consideration to minimize multiple mappings between any two mode groups. We note that the proposed scheme is one of the many possible schemes that are non-periodic for practical numbers of recirculations. Additionally, the proposed approach can easily be generalized to construct non-cyclic permutation schemes for multi-mode fibers supporting arbitrary number of modes.

It is instructive noting that in the ideal case where no coupling occurs during propagation in the MMF spans, the C-MP scheme would be optimal in terms of delay management. This is illustrated in Fig. 2, where we plot the *delay spread* (that is, the largest differential delay between any two modes) versus propagation distance both in the absence of MP and for each of the considered permutation schemes, under the assumption of uncoupled MMF propagation. For the plot we assumed numerical values extracted from the experiment. In particular, we assumed a 15-mode fiber link with a span length of 58.9 km and the differential mode-group delays (DMGDs) relative to the fundamental mode measured at 1557.8 nm. These are listed

TABLE I
DISPERSION COEFFICIENTS AT 1557.8 NM USED FOR SIMULATION

	$\mathbf{MG}_a$	$\mathbf{MG}_b$	$\mathbf{MG}_c$	$\mathbf{MG}_d$	$\mathbf{MG}_e$
MD γ_u (ps/km$^{1/2}$)	2.1369	13.304	8.0916	9.8246	16.952
DMGD β'_u (ps/km) (w.r.t. $\mathbf{MG}_a$)	–	−85.236	−67.219	−54.399	−68.951

in Table I, which is discussed in Section IV, along with other parameters that are not used in this section. The plot shows that, as expected, in the absence of MP the delay spread grows linearly with propagation distance (blue dots), and it coincides with the differential delay between the slowest and the fastest modes. In the case of C-MGP (crosses and triangles) and NC-MGP (plus symbols), it also grows linearly with propagation distance, yet with a lower growth rate. In contrast, the delay spread is bounded and periodic in the case of C-MP (squares), as a result of the fact that each mode accumulates the same propagation delay after a number of permutation stages equal to the number of modes.

This picture changes completely in the presence of random mode coupling. Indeed, the experimental and simulation results presented in the following sections show that in realistic regimes of intra-group and inter-group coupling all permutation schemes have similar performance. In simulations, the C-MP scheme is even slightly lower performing than the others, which aligns with the observation that this scheme is the least effective in enhancing inter-mode-group coupling, as it only couples a single mode of each group into a mode of an adjacent mode group.

III. EXPERIMENT

A. Experimental Setup

Fig. 3 illustrates the experimental setup employed to validate the efficacy of the examined mode permutation schemes. To generate a three-channel sliding test band, carriers from three tunable lasers (TLs) were modulated using two dual-polarization IQ-modulators (DP-IQMs). These modulators were driven by the same 65 GS/s 4-channel arbitrary waveform generator (AWG). The resulting modulated signals adopted the form of dual-polarization quadrature phase-shift keying (DP-QPSK) signals with a 1% roll-off root-raised cosine pulse shape, transmitted at a rate of 24.5 GBd. A dummy-band was generated by utilizing an optical processor (OP) to spectrally flatten the amplified spontaneous emission noise originating from an erbium-doped fiber amplifier. The composite signal, encompassing both the test and dummy bands, was passed through a loading acousto-optic modulator (AOM), acting as an optical switch, before undergoing a split and delay procedure to generate 15 uncorrelated replicas of the same signal. These replicas, characterized by a relative delay of 150 ns, were subsequently directed into 15 parallel recirculating loops with precisely aligned path lengths. The alignment of the 15 parallel recirculating loops was executed with a precision within the tolerance range of ± 1 cm, corresponding to a differential offset on the order of approximately ± 50 ps. The signals associated with each of the 15 loops were amplified and subsequently multiplexed using a multi-plane light converter (MPLC) [22].

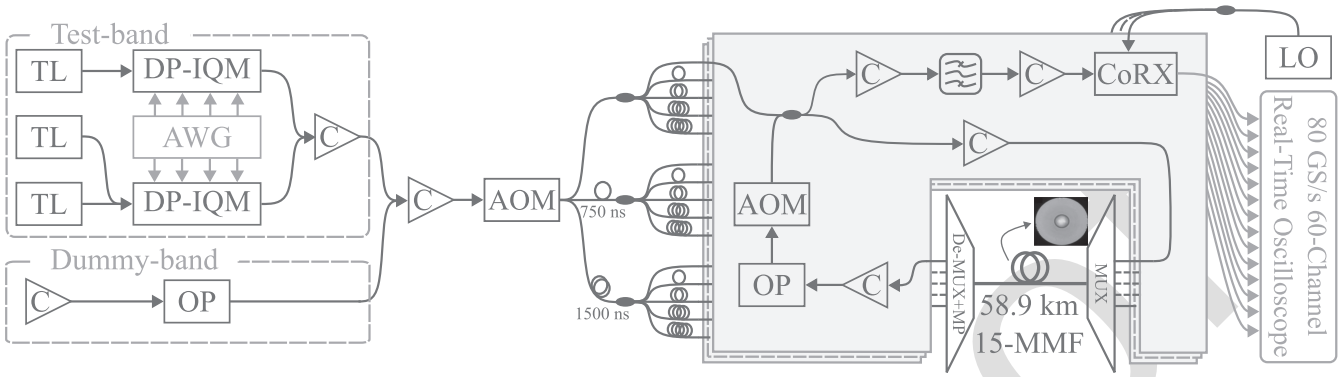

Fig. 3. Experimental setup of the recirculating-loop-based long-haul 15-mode fiber link. Mode permutation is performed at the de-multiplexing stage.

Following the multiplexing process, the combined signal was launched into a 58.9 km long span of 15-mode MMF with low loss (between 0.21 dB/km and 0.24 dB/km for the 15 spatial modes at 1550 nm) and inherently low DMGD (<100 ps/km at 1550 nm) [23]. The outputs of the MPLC de-multiplexer were connected to the single-mode loops based on the prescribed permutation schemes. Subsequently, the signals entered a second amplification stage, followed by OPs to rectify amplifier gain tilts as well as fiber and component loss profiles, and looping AOMs to implement recirculating-loop transmission. Regarding signal reception, the 15 outputs from the parallel loops were first amplified. Subsequently, the channel of interest (COI) was filtered and amplified once more before being received by 15 coherent receivers (CoRXs) that shared a common path-length aligned local oscillator (LO). The electrical signals were captured using an 80-GS/s 60-channel real-time oscilloscope, with the recorded traces intended for offline DSP, mainly involving a time-domain 30 × 30 MIMO equalizer. This required a time-domain equalizer window of 71.4 ns in the absence of MP, and of only 38.8 ns when MP was present in the case of recirculating-loop transmission.

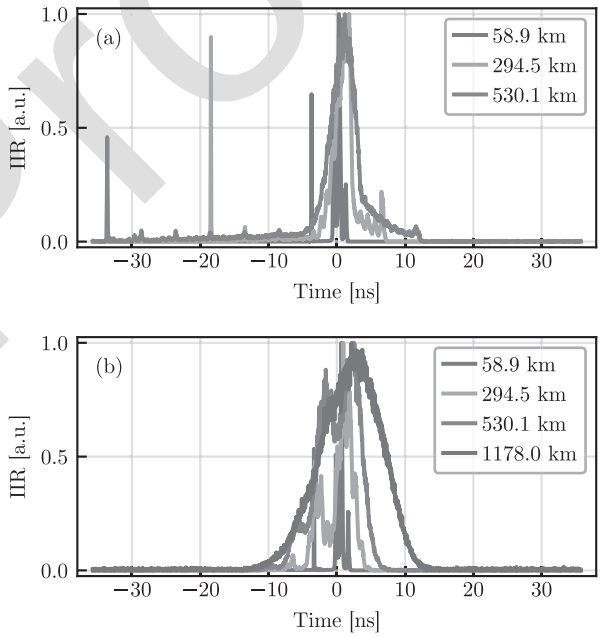

Fig. 4. Intensity impulse response for various transmission distances at 1557.8 nm (a) in the absence of MP and (b) with NC-MGP.

B. Experimental Results

1) Modal Dispersion Accumulation: Fig. 4(a) and (b) show how the shape of the IIR measured at 1557.8 nm evolves as propagation distance increases in the absence of MP and when NC-MGP is applied, respectively. Here, the IIR is defined as the sum of the absolute square values of the equalizer taps, normalized with respect to their maximum value. The isolated peaks seen in the first case are an indication of weak inter-group coupling occurring in the MMF spans, while their disappearance after a few spans in the second case is clearly a consequence of MP. Moreover, the Gaussian-shaped profile of the IIR at 1178 km is a signature of the strong mode coupling regime achieved in the presence of MP [17], [24].

In Fig. 5(a) we plot the duration of the IIR versus propagation distance for all permutation schemes, as well as in the absence of MP. Here, we define the IIR duration as the time interval encompassing 98% of the IIR energy, and each data point is obtained by averaging the IIR duration of the MMF link across five different wavelength channels spanning the C-band, specifically at 1533.9, 1539.8, 1545.7, 1553.7, and 1557.8 nm. The dots are obtained in the absence of MP and the straight line is a linear fit to the data, showing that in this case the IIR duration starts increasing linearly with propagation distance, as a result of the weak inter-mode-group coupling.[1] As inter-group coupling becomes non-negligible, a transition to a sub-linear growth of the IIR duration is seen, at approximately 400 km. The markers, complemented by a square-root data fit growing at a rate of approximately 496 ps/$\sqrt{\text{km}}$, refer to the considered permutation schemes. The remarkable alignment between the data and the square-root fit indicates that the MMF link is operating in the strong mode coupling regime, underscoring

[1]We acknowledge that the observed linear increase in the IIR duration with propagation distance, in the absence of mode permutation, may be attributed in part to certain loop artifacts–such as path-length misalignment between single-mode loops–that are inherently present in practical transmission systems. If this assumption holds true, our findings demonstrate the effective mitigation of these artifacts' impact through the implementation of mode permutation.

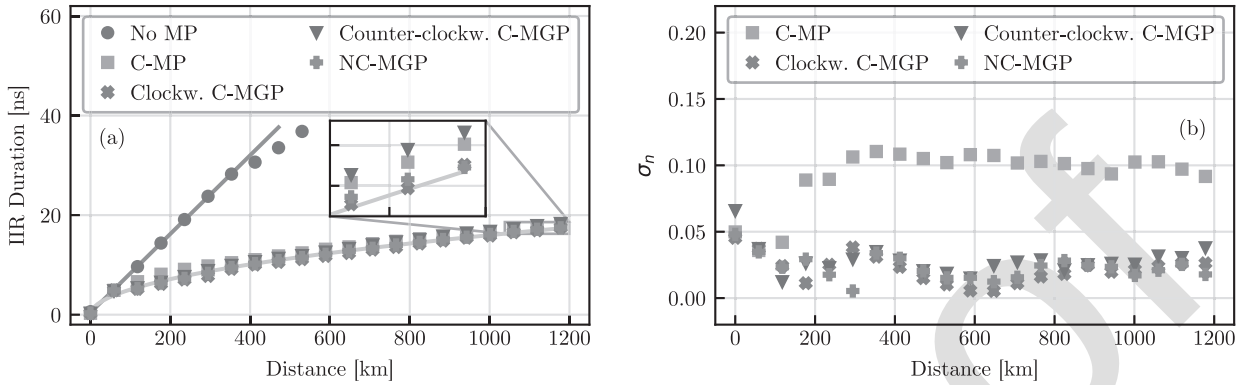

Fig. 5. (a) Wavelength-averaged IIR duration versus transmission distance in the absence of MP and for the considered permutation schemes and (b) normalized standard deviation of the IIR duration versus transmission distance for the considered permutation schemes. The line spacing in the inset of (a) is 2 ns.

the efficacy of the considered permutation schemes in facilitating inter-mode-group coupling. The performance among the schemes exhibits no significant differences, while an impressive reduction of approximately 65% in the IIR duration is obtained at 530.1 km. The fact that C-MP performs similar to the other schemes is in contrast with what was observed in [10]. We attribute this discrepancy to the fact that, in our case, C-MP always maps LP_{01} into LP_{11}, which are the fastest and the slowest mode groups,[2] respectively, at all wavelengths used in the experiment, therefore implementing a delay-management scheme that remains somewhat effective also in the presence of random mode coupling, beyond the ideal case of no-coupling illustrated in Fig. 2. However, this result would change if the first and the second mode groups were not the fastest and the slowest, respectively.

We also examined the wavelength dependence of the IIR duration. To this end, we calculated the normalized standard deviation of the IIR duration measured across the five distinct wavelength channels spanning the C-band for each permutation scheme. This is obtained by normalizing the actual standard deviation of the IIR duration with respect to its average value, namely $\sigma_n = \frac{1}{\mu}\sqrt{\frac{1}{N_{\mathrm{ch}}}\sum_{i=1}^{N_{\mathrm{ch}}}(T_i-\mu)^2}$, where T_i is the i-th wavelength-channel's IIR duration, and $\mu = \frac{1}{N_{\mathrm{ch}}}\sum_{i=1}^{N_{\mathrm{ch}}} T_i$ is the average duration across all channels. In Fig. 5(b), σ_n is plotted versus propagation distance for each permutation scheme. The plot shows that all permutation schemes have similar wavelength dependence,[3] with the exception of the C-MP scheme, which exhibits a stronger dependence on wavelength. We speculate that the larger deviation is due to the fact that the C-MP scheme is less effective in achieving strong mode coupling than the other schemes, which makes the profile and duration of the IIR not as deterministic as it would be expected [17].

2) MDL Accumulation: Modal dispersion is a unitary effect with no direct implications on the achievable data transmission capacity. In contrast, MDL is non-unitary and it fundamentally limits the achievable transmission performance [26], [27], [28],

[2]For the channel at 1558.8 nm, this can be seen in Table I.

[3]Specifically, in [25], the IIR duration is seen to increase as a function of wavelength.

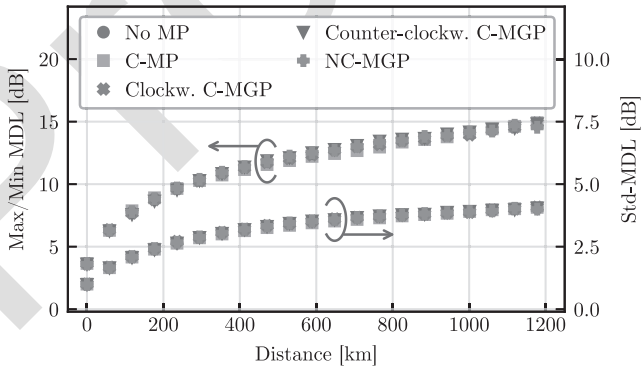

Fig. 6. Wavelength-averaged Max/Min MDL and Std-MDL versus propagation distance in the absence of MP and for the considered permutation schemes.

[29]. We characterize the link's MDL by using two metrics. The first metric is the ratio in dB between the largest and smallest eigenvalues of $\mathbf{H}(\omega)\mathbf{H}^{\dagger}(\omega)$, where by $\mathbf{H}(\omega)$ we denote the frequency-dependent transfer matrix of the MMF link and by $\mathbf{H}^{\dagger}(\omega)$ its hermitian adjoint. We refer to this metric as Max/Min MDL. The frequency-dependent transfer matrix $\mathbf{H}(\omega)$ is derived as the inverse of the Fourier transform of the time-domain MIMO equalization matrix. The second metric is the standard deviation of the natural logarithm of all of the eigenvalues of the same matrix, also expressed in dB [27]. We refer to this metric as Std-MDL. The frequency dependence of the so-evaluated quantities is then eliminated by performing a frequency average across the WDM channel bandwidth.

In Fig. 6, we plot the MDL of the 15-mode fiber link versus propagation distance for all the considered permutation schemes, as well as in the absence of MP. It is worth noting that the results in the absence of MP are hidden by the presence of the other data points. Similarly to what was done for the IIR duration, each data point is obtained by averaging the MDL of the MMF link across the five channel wavelengths. The vertical axis on the left refers to the Max/Min MDL, while the vertical axis on the right refers to the Std-MDL. The results in the latter figure show no substantial differences among the various permutation scenarios, indicating that MP does not affect the accumulation of MDL, in agreement with what was observed

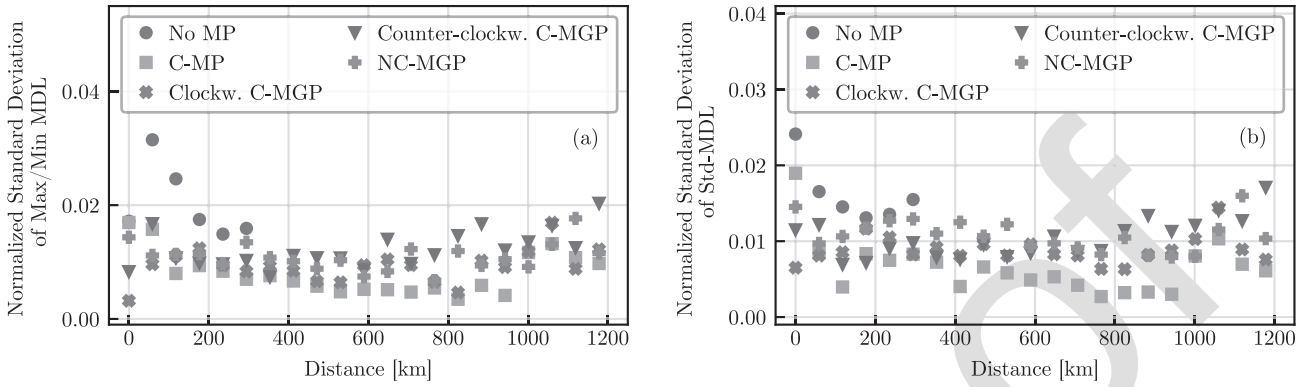

Fig. 7. Normalized standard deviation of (a) Max/Min MDL and (b) Std-MDL versus transmission distance in the absence of MP and for the considered permutation schemes.

in [30]. An interesting feature that emerges from the results of Fig. 6 is that MDL accumulates proportionally to the square root of propagation distance not only in the presence of MP, but also when no MP is implemented. This result comes as a surprise, as one would expect to see a linear growth of MDL with propagation distance. A possible explanation of this behavior is that MDL is dominated by some intra-mode-group MDL, possibly arising from the in-span fiber splices, rather than by inter-mode-group MDL. In particular, we have verified that the MDL values extracted from the channel-transfer-matrix blocks describing the fourth and fifth mode groups after one fiber span are comparable in magnitude to the overall MDL. On the other hand, MDL measurements performed on a deployed 48 km-long fiber of the same kind used in this work have shown that when addressing only the fourth fiber mode-group [31] or all the fiber modes [32], the measured MDL values are quite similar. These evidences provide a qualitative explanation of why MDL grows proportionally with the square root of propagation distance, namely because its accumulation is dominated by strong coupling within a group of quasi-degenerate modes.

We also characterized the wavelength dependence of MDL. To this end, we computed the normalized standard deviation of the MDL measured across the five distinct wavelength channels spanning the C-band for each permutation scheme. Fig. 7 shows the resulting values of the normalized standard deviation plotted versus the transmission distance in the absence of MP and for all the considered permutation schemes, with Fig. 7(a) referring to the Max/Min MDL, and Fig. 7(b) to the Std-MDL. The absence of substantial difference between the considered scenarios is consistent with the argument that MDL accumulation is dominated by intra-mode-group dynamics.

IV. Simulations

In this section we perform simulations in support of the experimental results, with two main goals. On the one hand, we aim to assess whether the similarity in performance between the considered permutation schemes is consistent with some simple and fully-controllable model or results from practical implementation aspects. On the other hand, we aim to assess whether the performance of MP improves in real systems, where the signal propagates in uncorrelated fiber spans, as compared to the case where it propagates in the same fiber span in a recirculating-loop configuration.

A. Model for Distributed Coupling and Parameter Extraction

We start by considering two non-degenerate mode groups a and b, which we describe by means of generalized Jones vectors $\vec{E}_a$ and $\vec{E}_b$ [16], whose evolution along the fiber obeys the following set of coupled equations,

$$\frac{\mathrm{d}\vec{E}_a}{\mathrm{d}z} = i\beta_a\vec{E}_a + i\omega\beta'_a\vec{E}_a + i\frac{\vec{V}_a\cdot\vec{\Lambda}_a}{2N_a}\vec{E}_a + i\omega\frac{\vec{W}_a\cdot\vec{\Lambda}_a}{2N_a}\vec{E}_a - \frac{\alpha_a}{2}\vec{E}_a - \frac{\vec{\alpha}_a\cdot\vec{\Lambda}_a}{2} + i\mathbf{C}\vec{E}_b \quad (1)$$

$$\frac{\mathrm{d}\vec{E}_b}{\mathrm{d}z} = i\beta_b\vec{E}_b + i\omega\beta'_b\vec{E}_b + i\frac{\vec{V}_b\cdot\vec{\Lambda}_b}{2N_b}\vec{E}_b + i\omega\frac{\vec{W}_b\cdot\vec{\Lambda}_b}{2N_b}\vec{E}_b - \frac{\alpha_b}{2}\vec{E}_b - \frac{\vec{\alpha}_b\cdot\vec{\Lambda}_b}{2} + i\mathbf{C}^\dagger\vec{E}_a. \quad (2)$$

Here β_u and β'_u, with $u \in \{a, b\}$, are the propagation constant and its derivative with respect to the angular frequency ω, respectively, for mode group u, while N_u is the number of degenerate spatial modes in the same group. By $\vec{V}_u$ we denote a generalized Stokes vector of dimension $D_u = 4N_u^2 - 1$, while by $\vec{\Lambda}_u$ we denote a vector whose elements are $2N_u \times 2N_u$ generalized Pauli matrices, so that $\vec{V}_u \cdot \vec{\Lambda}_u = \sum_{n=1}^{D_u} V_{u,n}\Lambda_{u,n}$ [16]. This term describes intra-group random mode coupling in mode groups u. The vector $\vec{W}_u$ is also a generalized Stokes vector and it describes intra-group modal dispersion [16]. The matrix $\mathbf{C}$ and its Hermitian adjoint $\mathbf{C}^\dagger$ account for random inter-group coupling. By α_a and α_b we denote the mode-group averaged loss coefficients, while the vectors $\vec{\alpha}_a$ and $\vec{\alpha}_b$ are the local MDL vectors, which we also model as independent white-noise processes of suitable strength [28]. In what follows, we model both intra-group and inter-group random coupling by means of white noise processes, with the result that the mismatch in propagation constant becomes immaterial and the terms proportional to β_u can be dropped [33]. A further simplification is obtained by establishing a reference frame that

follows intra-group coupling in each mode group. This yields the following simplified equations

$$\frac{\mathrm{d}\vec{E}_a}{\mathrm{d}z} = i\omega\beta_a'\vec{E}_a + i\omega\frac{\vec{W}_a\cdot\vec{\Lambda}_a}{2N_a}\vec{E}_a - \frac{\alpha_a}{2}\vec{E}_a - \frac{\vec{\alpha}_a\cdot\vec{\Lambda}_a}{2} + i\mathbf{C}\vec{E}_b \tag{3}$$

$$\frac{\mathrm{d}\vec{E}_b}{\mathrm{d}z} = i\omega\beta_b'\vec{E}_b + i\omega\frac{\vec{W}_b\cdot\vec{\Lambda}_b}{2N_b}\vec{E}_b - \frac{\alpha_b}{2}\vec{E}_b - \frac{\vec{\alpha}_b\cdot\vec{\Lambda}_b}{2} + i\mathbf{C}^\dagger\vec{E}_a, \tag{4}$$

with

$$\langle W_{u,i}(z)W_{u,j}(z')\rangle = \gamma_u^2\delta_{i,j}\delta(z-z') \tag{5}$$

$$\langle \alpha_{u,i}(z)\alpha_{u,j}(z')\rangle = \zeta_u^2\delta_{i,j}\delta(z-z') \tag{6}$$

$$\langle C_{i,j}(z)C^*_{i',j'}(z')\rangle = \eta^2\delta_{i,i'}\delta_{j,j'}\delta(z-z') \tag{7}$$

$$\langle C_{i,j}(z)C_{i',j'}(z')\rangle = 0, \tag{8}$$

where the coefficients involved are to be extracted from the experimental data. The inverse group velocities β_u' are obtained by inspecting the peaks of the measured IIR after propagation in the first fiber span.

The MD coefficients γ_u^2 are known to be related to the duration of the intra-group intensity impulse responses through the relation $T_u^2(z) = \gamma_u^2 D_u/4N_u^2\, z$ [17]. This allows to extract them by fitting the intensity impulse responses of the individual mode groups at the output of the first fiber span with a Gaussian-shaped waveform with root-mean-square width equal to T_u.

We set $\alpha_a = \alpha_b = 0$ and $\vec{\alpha}_a = \vec{\alpha}_b = 0$ in the following discussion. We leave the analysis of MDL accumulation to Section IV-D.

The extraction of the inter-group coupling coefficients is more involved. Here we proceed by evaluating the evolution of the mean optical powers in the individual mode groups, as these quantities can be extracted from the experimental crosstalk matrix. To this end we make use of the Ito calculus [34], by first expressing (3) and (4) in the Stratonovich form, namely,

$$\mathrm{d}\vec{E}_a = i\omega\beta_a'\vec{E}_a\mathrm{d}z + i\omega\frac{\mathrm{d}\vec{W}_a\cdot\vec{\Lambda}_a}{2N_a}\vec{E}_a + i\mathrm{d}\mathbf{C}\vec{E}_b \tag{9}$$

$$\mathrm{d}\vec{E}_b = i\omega\beta_b'\vec{E}_b\mathrm{d}z + i\omega\frac{\mathrm{d}\vec{W}_b\cdot\vec{\Lambda}_b}{2N_b}\vec{E}_b + i\mathrm{d}\mathbf{C}^\dagger\vec{E}_a. \tag{10}$$

The Ito-corrected equations are obtained in the following form with the use of (5), (7) and (8),

$$\mathrm{d}\vec{E}_a = i\omega\beta_a'\vec{E}_a\mathrm{d}z + i\omega\frac{\mathrm{d}\vec{W}_a\cdot\vec{\Lambda}_a}{2N_a}\vec{E}_a + i\mathrm{d}\mathbf{C}\vec{E}_b - \omega^2\frac{\gamma_a^2 D_a}{8N_a^2}\vec{E}_a\mathrm{d}z - \frac{1}{2}\eta^2 2N_b\vec{E}_a\mathrm{d}z \tag{11}$$

$$\mathrm{d}\vec{E}_b = i\omega\beta_b'\vec{E}_b\mathrm{d}z + i\omega\frac{\mathrm{d}\vec{W}_b\cdot\vec{\Lambda}_b}{2N_b}\vec{E}_b + i\mathrm{d}\mathbf{C}^\dagger\vec{E}_a - \omega^2\frac{\gamma_b^2 D_b}{8N_b^2}\vec{E}_b\mathrm{d}z - \frac{1}{2}\eta^2 2N_a\vec{E}_b\mathrm{d}z. \tag{12}$$

The equations for the average powers carried by each mode group $I_a = \langle\vec{E}_a^\dagger\vec{E}_a\rangle$ and $I_b = \langle\vec{E}_b^\dagger\vec{E}_b\rangle$ are then obtained in the following form,

$$\mathrm{d}I_a = \eta^2 2N_a I_b\mathrm{d}z - \eta^2 2N_b I_a\mathrm{d}z \tag{13}$$

$$\mathrm{d}I_b = \eta^2 2N_b I_a\mathrm{d}z - \eta^2 2N_a I_b\mathrm{d}z, \tag{14}$$

or, equivalently,

$$\frac{\mathrm{d}}{\mathrm{d}z}\begin{bmatrix} I_a \\ I_b\end{bmatrix} = \begin{bmatrix} -2\eta^2 N_b & 2\eta^2 N_a \\ 2\eta^2 N_b & -2\eta^2 N_a\end{bmatrix}\begin{bmatrix} I_a \\ I_b\end{bmatrix} = \mathbf{K}\begin{bmatrix} I_a \\ I_b\end{bmatrix}. \tag{15}$$

The solution to the above,

$$\begin{bmatrix} I_a(z) \\ I_b(z)\end{bmatrix} = \exp(\mathbf{K}z)\begin{bmatrix} I_a(0) \\ I_b(0)\end{bmatrix} = \mathbf{X}_g\begin{bmatrix} I_a(0) \\ I_b(0)\end{bmatrix}, \tag{16}$$

can be mapped into experimental data, by establishing a relation between the matrix $\mathbf{X}_g$, which describes inter-mode-group crosstalk, and the experimentally measurable crosstalk matrix $\mathbf{X}$. This relation is not straightforward and is discussed in what follows. Prior to doing so, however, we note that the expression of $\mathbf{K}$ can be readily generalized to the case of more than two mode groups. For instance, in the case of three mode groups a, b, and c, it takes the following form

$$\begin{bmatrix} -2(\eta_{ab}^2 N_b + \eta_{ac}^2 N_c) & 2\eta_{ab}^2 N_a & 2\eta_{ac}^2 N_a \\ 2\eta_{ab}^2 N_b & -2(\eta_{ab}^2 N_a + \eta_{bc}^2 N_c) & 2\eta_{bc}^2 N_b \\ 2\eta_{ac}^2 N_c & 2\eta_{bc}^2 N_c & -2(\eta_{ac}^2 N_a + \eta_{bc}^2 N_b)\end{bmatrix} \tag{17}$$

where η_{uv}^2 is the coefficient that describes coupling between mode groups u and v. Fig. 8 illustrates the relation between $\mathbf{X}_g$, which is a $N_g \times N_g$ matrix (with N_g denoting the number of non-degenerate mode groups), and $\mathbf{X}$, which is an $N \times N$ matrix (with N denoting the total number of modes), in the case of a three-mode-group fiber. The figure relies on the fact that the simple model used in this work yields a crosstalk matrix $\mathbf{X}$ that is symmetric and made of blocks with identical elements[4] (the elements in each block are identical owing to the strong intra-group mixing). Therefore, each element in the mode-group

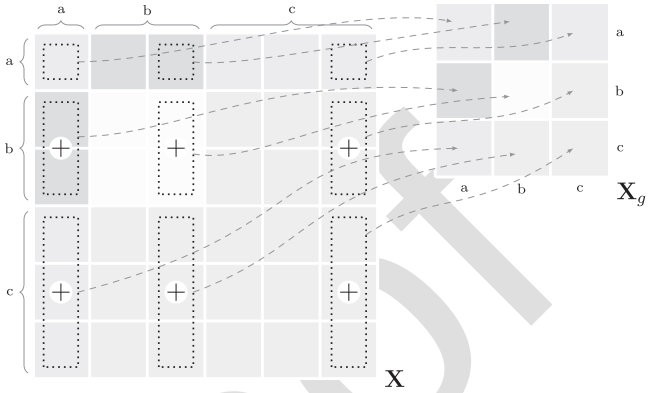

Fig. 8. Relation between the $N \times N$ crosstalk matrix $\mathbf{X}$ and the $N_g \times N_g$ matrix $\mathbf{X}_g$ describing inter-mode-group crosstalk, in the example of a three-mode-group fiber, where $N = 6$ and $N_g = 3$.

[4]Symmetry emerges immediately in the special case $N_a = N_b = N_c = 1$, where $\mathbf{X}$ and $\mathbf{X}_g$ coincide.

TABLE II
COUPLING COEFFICIENTS AT 1557.8 NM USED FOR SIMULATION

Coefficient	Value ($\mathrm{km}^{-1/2}$)	Coefficient	Value ($\mathrm{km}^{-1/2}$)
η_{ab}	0.0296	η_{bd}	0.0144
η_{ac}	0.0130	η_{be}	0.0129
η_{ad}	0.0297	η_{cd}	0.0150
η_{ae}	0.0129	η_{ce}	0.0302
η_{bc}	0.0147	η_{de}	0.0325

crosstalk matrix $\mathbf{X}_g$ corresponding to a specific pair of mode groups is obtained by summing the elements of any one column of $\mathbf{X}$ that also corresponds to the same pair of mode groups. For instance, the (b, c) element of $\mathbf{X}_g$ can be obtained by summing the second and third elements of the sixth column of $\mathbf{X}$ (or, equivalently, the second and third elements of the fourth or the fifth column of $\mathbf{X}$). Note that all the elements in each column (or row) of $\mathbf{X}$ sum to unity, as a result of unitary propagation assumed in the model.

Extracting the 5×5 matrix $\mathbf{X}_g$ from the experimental 15×15 crosstalk matrix $\mathbf{X}_{\text{exp}}$ is not as straightforward, as in practice $\mathbf{X}_{\text{exp}}$ never takes the highly symmetric form illustrated in Fig. 8. Note that by $\mathbf{X}_{\text{exp}}$ we denote the time- and polarization-averaged absolute square fiber impulse response matrix, measured for a single MMF span. The first step towards extracting the ten coupling coefficients (one per each pair of mode groups) is therefore enforcing this form into $\mathbf{X}_{\text{exp}}$, which is done as follows. The matrix $\mathbf{X}_{\text{exp}}$ is first normalized so that the sum of each column's elements equals one. The obtained matrix (that in practice is slightly asymmetric) is then symmetrized into $\tilde{\mathbf{X}}_{\text{exp}} = (\mathbf{X}_{\text{exp}} + \mathbf{X}_{\text{exp}}^t)/2$. To shape $\tilde{\mathbf{X}}_{\text{exp}}$ into the form depicted in Fig. 8, all the elements within each of the off-diagonal blocks are replaced with their respective averages. Subsequently, normalization of each column is re-enforced by setting the elements in each diagonal square box with identical values so that the sum of the elements in each column equals one. The resulting matrix can then be used to extract $\mathbf{X}_g$ as illustrated in Fig. 8, and the ten coupling coefficients are obtained from the off-diagonal elements of $\log(\mathbf{X}_g)/L_s$, where L_s is the span length.

B. Numerical Simulation

In the numerical simulation, propagation is modeled based on (3) and (4), generalized for five mode groups. A 15-mode fiber span of length $L_s = 58.9$ km (consistent with the experiment) is emulated. It is implemented as a concatenation of $\mathcal{N} = 400$ wave-plates of width $\Delta z = L_s/\mathcal{N}$. The transfer matrix of each wave-plate $\mathbf{U}_{\text{wp}}$ is then characterized by $\exp(i\mathbf{M}\Delta z)$, with

$$\mathbf{M} = \begin{bmatrix} \frac{\vec{W}_a \cdot \vec{\Lambda}_a}{2N_a}\omega & \mathbf{C}_{ab} & \mathbf{C}_{ac} & \mathbf{C}_{ad} & \mathbf{C}_{ae} \\ \mathbf{C}_{ab}^\dagger & \frac{\vec{W}_b \cdot \vec{\Lambda}_b}{2N_b}\omega & \mathbf{C}_{bc} & \mathbf{C}_{bd} & \mathbf{C}_{be} \\ \mathbf{C}_{ac}^\dagger & \mathbf{C}_{bc}^\dagger & \frac{\vec{W}_c \cdot \vec{\Lambda}_c}{2N_c}\omega & \mathbf{C}_{cd} & \mathbf{C}_{ce} \\ \mathbf{C}_{ad}^\dagger & \mathbf{C}_{bd}^\dagger & \mathbf{C}_{cd}^\dagger & \frac{\vec{W}_d \cdot \vec{\Lambda}_d}{2N_d}\omega & \mathbf{C}_{de} \\ \mathbf{C}_{ae}^\dagger & \mathbf{C}_{be}^\dagger & \mathbf{C}_{ce}^\dagger & \mathbf{C}_{de}^\dagger & \frac{\vec{W}_e \cdot \vec{\Lambda}_e}{2N_e}\omega \end{bmatrix}. \tag{18}$$

As discussed in the previous section, the terms in the main diagonal describe intra-group mode dispersion. The vectors $\vec{W}_u$ $(u \in \{a, b, c, d, e\})$ are all independently generated and their components are independent Gaussian random variables with zero mean and standard deviation equal to $\gamma_u/\sqrt{\Delta z}$, consistent with (5). The matrix $\mathbf{C}_{uv}$ $(u, v \in \{a, b, c, d, e\})$ describes coupling between mode groups u and v. The coupling matrices are generated independently of one another and, in accordance with (7) and (8), their elements are independent complex-valued Gaussian random variables with zero mean, uncorrelated real and imaginary parts, and standard deviation equal to $\eta_{uv}/\sqrt{\Delta z}$.

Consistently with the experimental settings, the fiber-span transfer matrix $\mathbf{T}_s(\omega)$ is calculated in a frequency band of 24.5 GHz. Multiple recirculations are described in the frequency domain by the matrix $\mathbf{T}_s(\omega)\mathbf{P}\mathbf{T}_s(\omega)\cdots\mathbf{P}\mathbf{T}_s(\omega)$, where by $\mathbf{P}$ we denote a 30×30 matrix that implements ideal MP. The inverse Fourier transform of the accumulating matrix is used to evaluate the intensity impulse response at every recirculation. The parameters used in the simulations for the wavelength channel at 1557.8 nm are listed in Tables I and II.

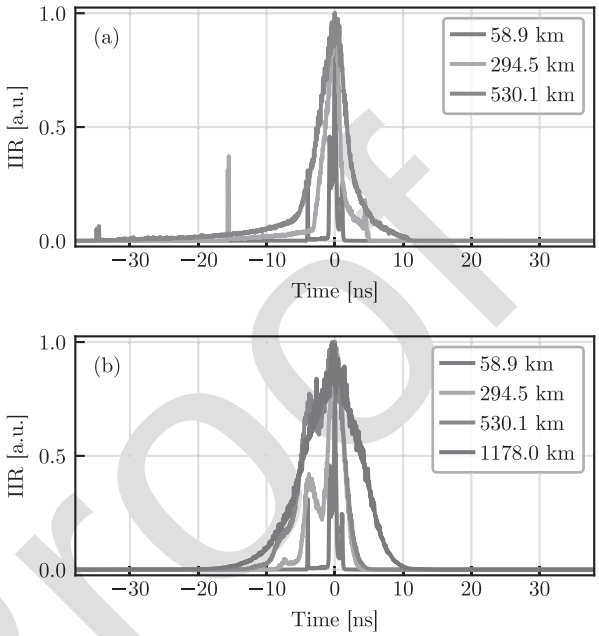

Fig. 9. Simulated IIR for various transmission distances at 1557.8 nm (a) in the absence of MP and (b) with NC-MGP.

C. Simulation Results: Modal Dispersion

Fig. 9 shows a plot of the simulated IIR of the wavelength channel at 1557.8 nm, for the same propagation distances and MP settings as in Fig. 4. A qualitative similarity between the two figures can be noticed.

Fig. 10(a) shows the plot of the IIR duration versus propagation distance for the same wavelength channel (the duration of the simulated IIR is calculated to be the period of time which encompasses 98% of the IIR energy, as in the experiment). Similarly, Fig. 10(b) illustrates the extension of the same analysis to all five channels, with their average IIR duration plotted versus propagation distance. In both figures, a square-root fit is also plotted for comparison. The plot indicates that, on average, all

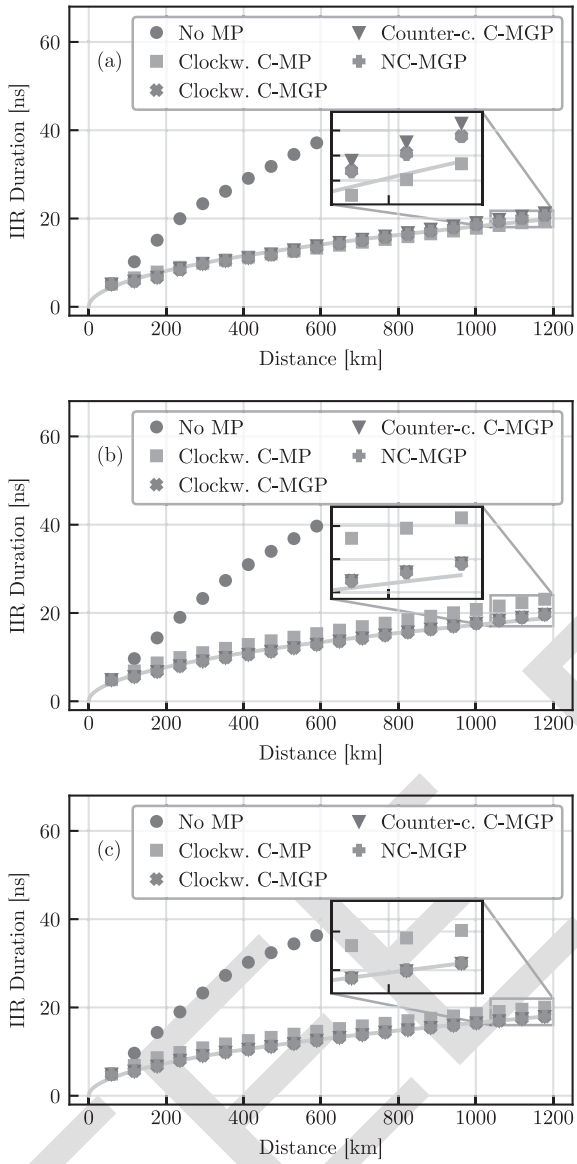

Fig. 10. (a) Simulated-IIR duration of the wavelength channel at 1557.8 nm versus propagation distance in the recirculating-loop configuration. (b) Simulated-IIR duration averaged over the five wavelength channels used in the experiment versus propagation distance in the recirculating-loop configuration. (c) Same as in (b) for a link with independent fiber spans. The line spacings in the insets of (b) and (c) are 2 ns.

permutation schemes yield similar results in remarkable agreement with the experiment, with the C-MP scheme, performing slightly lower than the others. Specifically, at 1178 km, it results in an IIR duration approximately 2 ns greater than for the other schemes. This suggests that in the propagation regime of our experiment, inter-group coupling is more critical than delay management in implementing MP. The fact that no difference in performance between the C-MP scheme and the other schemes is observed experimentally, must be ascribed to additional coupling introduced in the experimental setup. Indeed, in our model we assume that coupling occurs only during fiber propagation, whereas multiplexing, de-multiplexing and MP are implemented ideally, that is by introducing no additional cross-talk.

We used the model developed for propagation in the 15-mode fiber, to evaluate the performance of the permutation schemes in a realistic multi-span fiber system, where permutation is performed between independent fiber spans. To this end, we simulated a fiber link composed of 20 fiber spans, where each span was generated independently as described above. Fig. 10(c) illustrates the IIR duration evaluated at the end of each span for all permutation schemes. Note that, similar to Fig. 10(b), each data point in the figure is obtained by averaging the IIR duration of the MMF link across the five wavelength channels spanning the C-band. Compared to the recirculating-loop configuration, only a small additional reduction in the IIR duration is observed, which further supports the reliability of our experimental findings in predicting the performance of MP in field-deployed multi-span fiber links.

It is worth stressing that the effectiveness of the C-MP scheme is strongly influenced by the fact that the fastest mode (LP_{01}) is always mapped into the slowest mode group (LP_{11}). This suggests a dependence on the details of the MMF design for this scheme's performance. Indeed, we verified through simulations that exchanging the group velocities of the five mode groups may substantially deteriorate the performance of the C-MP scheme, while having negligible practical impact on the performance of the other schemes.

D. Simulation Results: Mode-Dependent Loss

As observed in Section III-B2, MDL accumulates with propagation distance in the same way with and without MP. A possible explanation for this evidence is that MDL accumulates within groups of strongly coupled modes as a result of random and distributed local MDL, compatible with multiple fiber splices, thereby growing proportionally to the square root of propagation distance even in the absence of MP. Independence of the MDL accumulation on the mode permutation scheme has also been reported in [30], where it was argued that this might follows from the fact that MDL is mainly introduced by the single-mode stages connecting two recirculating loops.

To assess which one of the two assumptions is consistent with the experimental observations, we describe the accumulation of distributed MDL at the center frequency by simply setting $\omega = 0$ in (3) and (4). Conversely, we account for the case of MDL introduced by the single-mode stage by adding independent gain fluctuations with a Gaussian distribution and suitable strength to the propagating space and polarization modes between two recirculations, while assuming that the multimode fiber itself is unitary, that is, assuming $\alpha_a = \alpha_b = 0$ in (3) and (4). In both cases, a random phase is applied to each space and polarization mode between two recirculations, in order to account for the effect of the AOMs that are used in the loop as optical switches (the AOMs apply an 80 MHz frequency shift when they route the impinging signal towards the next circulation). Note that while the local MDL and the gain fluctuations are *frozen* from recirculation to recirculation, the random phases change from recirculation to recirculation as a result of the linewidth (resulting from frequency fluctuations) of the modulation applied by the AOMs. It is worth noting that the AOMs play an important

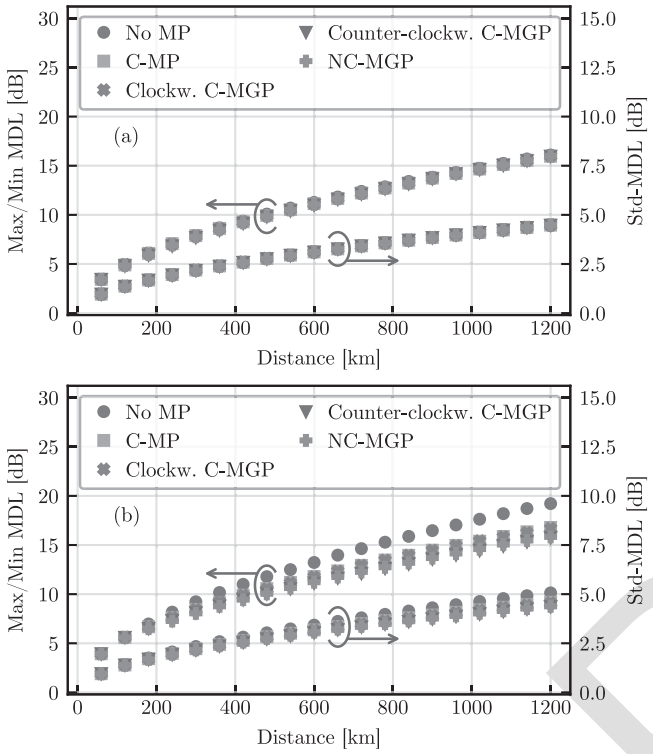

Fig. 11. Simulated Max/Min MDL and Std-MDL for the wavelength channel at 1557.8 nm versus propagation distance in the recirculating-loop configuration assuming (a) Distributed MDL, and (b) Single-mode gain fluctuations.

role in shaping the growth of MDL with propagation distance. In fact, this approaches a quasi-linear accumulation if no phase fluctuation is introduced, as is the case when electro-optic modulators are used as optical switches [35].

The simulation results are shown in Fig. 11, where we plot the average MDL versus propagation distance in the absence of mode permutation and for the considered MP schemes. The averaging is performed over 1000 link transfer matrices obtained for as many independent instantiations of the random quantities involved. Fig. 11(a) refers to the case of distributed MDL, and Fig. 11(b) to the case of single-mode gain fluctuations. Intra-group coupling was introduced so as to enforce a decorretalation length of 1km in each mode group [33]. For the inter-mode group coupling we assumed the coefficient values in Table II. For the local MDL strength, which is characterized by the coefficients ζ_u defined through (6), we assumed one of the many sets of numerical values that are compatible with an accumulated mean MDL of approximately 15 dB after 1200 km, as observed in the experiment. Finally, for the gain fluctuations, based on the same criterion, we assumed a standard deviation of 0.5 dB.

Inspection of Fig. 11 suggests that while MDL accumulation is similar across all considered schemes in both models, the model based on distributed MDL is more consistent with the experimental finding. Therefore, we conclude that distributed random MDL, possibly arising from fiber splices (seven in the experiment, one every less than 8 km in the loop), may be the predominant (yet not the only one) mechanism contributing to MDL accumulation in MMF links.

V. Conclusion

We experimentally investigated the effectiveness of four mode-permutation schemes in reducing the accumulation of modal dispersion in a long-haul 15-mode fiber link. We found that with mode permutation, the duration of the intensity impulse response of the MMF link increased proportionally to the square root of transmission distance, rather than linearly with it, as is the case in the absence of mode permutation. This reduced considerably the complexity of the receiver MIMO-DSP. We estimated an extension of the system reach from 530 km to 1178 km, enabled by a reduction in the time-domain equalizer window from 71.4 ns to 38.8 ns. Although no transmission results are shown in this work, such an extension has been demonstrated with a full C-band transmission in ref. [25]. The considered permutation schemes exhibited comparable performance with little wavelength dependence across the C-band. We also developed a simple model to simulate propagation in multi-mode fibers, whose parameters can be conveniently extracted from the experimental data. Simulations indicate negligible difference between the experimental results obtained in a recirculating-loop configuration and the performance of mode permutation in a realistic fiber link composed of independent fiber spans.

References

[1] P. J. Winzer and D. T. Neilson, "From scaling disparities to integrated parallelism: A decathlon for a decade," *J. Lightw. Technol.*, vol. 35, no. 5, pp. 1099–1115, Mar. 2017.

[2] A. Chraplyvy, "Plenary paper: The coming capacity crunch," in *Proc. IEEE 35th Eur. Conf. Opt. Commun.*, 2009, p. 1.

[3] B. J. Puttnam, G. Rademacher, and R. S. Luís, "Space-division multiplexing for optical fiber communications," *Optica*, vol. 8, no. 9, pp. 1186–1203, 2021. [Online]. Available: https://opg.optica.org/optica/abstract.cfm?URI=optica-8-9-1186

[4] S. Matsuo et al., "High-spatial-Multiplicity multicore fibers for future dense space-division-multiplexing systems," *J. Lightw. Technol.*, vol. 34, no. 6, pp. 1464–1475, Mar. 2016.

[5] R. Ryf et al., "Mode-division multiplexing over 96 km of few-mode fiber using coherent 6 MIMO processing," *J. Lightw. Technol.*, vol. 30, no. 4, pp. 521–531, Feb. 2012.

[6] N. K. Fontaine et al., "3030 MIMO transmission over 15 spatial modes," presented at Opt. Fiber Commun. Conf. Post Deadline Papers, Los Angeles, CA, USA, Mar. 22–26, 2015, Paper Th5C.1. [Online]. Available: https://opg.optica.org/abstract.cfm?URI=OFC-2015-Th5C.1

[7] G. Rademacher et al., "Peta-bit-per-second optical communications system using a standard cladding diameter 15-mode fiber," *Nature Commun.*, vol. 12, no. 1, 2021, Art. no. 4238, doi: 10.1038/s41467-021-24409-w.

[8] G. Rademacher et al., "1.53 peta-bit/s C-band transmission in a 55-Mode fiber," in *Proc. Eur. Conf. Opt. Commun.*, 2022, pp. 1–4. [Online]. Available: https://opg.optica.org/abstract.cfm?URI=ECEOC-2022-Th3C.3

[9] K. Shibahara et al., "DMD-Unmanaged long-haul SDM transmission over 2500-km 12-Core 3-Mode MC-FMF and 6300-km 3-mode FMF employing intermodal interference canceling technique," *J. Lightw. Technol.*, vol. 37, no. 1, pp. 138–147, Jan. 2019. [Online]. Available: https://opg.optica.org/jlt/abstract.cfm?URI=jlt-37-1-138

[10] K. Shibahara et al., "Long-haul DMD-Unmanaged 6-Mode-Multiplexed transmission employing cyclic mode-group permutation," in *Proc. IEEE Opt. Fiber Commun. Conf.*, 2020, pp. 1–3. [Online]. Available: https://opg.optica.org/abstract.cfm?URI=OFC-2020-Th3H.3

[11] K. Shibahara, M. Hoshi, and Y. Miyamoto, "10-spatial-mode 1300-km transmission over 6-LP graded index few-mode fiber with 36-ns modal dispersion," presented at Proc. Opt. Fiber Commun. Conf., San Diego, CA, USA, Mar. 5–9, 2023, p. M2B.2. [Online]. Available: https://opg.optica.org/abstract.cfm?URI=OFC-2023-M2B.2

[12] M. v. d. Hout et al., "273.6 Tb/s transmission over 1001 km of 15-Mode fiber using 16-QAM C-band signals," in *2023 Opt. Fiber Commun. Conf. Exhib.*, 2023, pp. 1–3.

[13] G. D. Sciullo et al., "Modal dispersion mitigation in a long-haul 15-Mode fiber link through mode permutation," in *2023 IEEE Photon. Soc. Summer Topicals Meeting Ser.*, 2023, pp. 1–2.
[14] X. Liu, Y. Wang, Q. Huang, and D. Zhang, "A joint mode permutation architecture for 10-Mode-Multiplexed long-haul transmissions," in *2024 Opt. Fiber Commun. Conf. Exhib.*, 2024, pp. 1–3.
[15] Y. Wang, X. Liu, Q. Huang, and D. Zhang, "10-mode PM-QPSK transmission over 2320 km enabled by optimized mode permutation strategies," presented at Opt. Fiber Commun. Conf. Exhib., San Diego, CA, USA, Mar. 24–28, 2024, Paper Th1H.7.
[16] C. Antonelli, A. Mecozzi, M. Shtaif, and P. J. Winzer, "Stokes-space analysis of modal dispersion in fibers with multiple mode transmission," *Opt. Exp.*, vol. 20, no. 11, pp. 11718–11733, 2012. [Online]. Available: https://opg.optica.org/oe/abstract.cfm?URI=oe-20-11-11718
[17] A. Mecozzi, C. Antonelli, and M. Shtaif, "Intensity impulse response of SDM links," *Opt. Exp.*, vol. 23, no. 5, pp. 5738–5743, 2015. [Online]. Available: http://www.osapublishing.org/oe/abstract.cfm?URI=oe-23-5-5738
[18] S. O. Arik, K.-P. Ho, and J. M. Kahn, "Group delay management and multiinput multioutput signal processing in mode-division multiplexing systems," *J. Lightw. Technol.*, vol. 34, no. 11, pp. 2867–2880, Jun. 2016. [Online]. Available: https://opg.optica.org/jlt/abstract.cfm?URI=jlt-34-11-2867
[19] G. Di Sciullo et al., "Reduction of modal dispersion in a long-haul 15-mode fiber link by means of mode permutation," in *Proc. 49th Eur. Conf. Opt. Commun.*, 2023, vol. 2023, pp. 250–253.
[20] A. Gatto et al., "Partial MIMO-based mode division multiplexing transmission over the first field-deployed 15-Mode fiber in metro scenario," in *2023 Opt. Fiber Commun. Conf. Exhib.*, 2023, pp. 1–3.
[21] P. Parolari et al., "Demonstration of multi-hop mode-group routing in a field-deployed multi-mode fiber network," in *2023 Opt. Fiber Commun. Conf. Exhib.*, 2023, pp. 1–3.
[22] N. K. Fontaine et al., "Broadband 15-Mode multiplexers based on multi-plane light conversion with 8 planes in unwrapped phase space," presented at Proc. Eur. Conf. Opt. Commun., Basel, Switzerland, Sep. 18–22, 2022, Paper We3A.2. [Online]. Available: https://opg.optica.org/abstract.cfm?URI=ECEOC-2022-We3A.2
[23] P. Sillard et al., "Low-differential-mode-group-delay 9-LP-mode fiber," *J. Lightw. Technol.*, vol. 34, no. 2, pp. 425–430, Jan. 2016.
[24] R. Ryf et al., "Space-division multiplexed transmission over 4200-km 3-Core microstructured fiber," presented at Proc. Nat. Fiber Optic Eng. Conf., Los Angeles, CA, USA, 2012, Paper PDP5C.2. [Online]. Available: https://opg.optica.org/abstract.cfm?URI=NFOEC-2012-PDP5C.2
[25] M. van den Hout et al., "Transmission of 273.6 Tb/s over 1001 km of 15-Mode multi-mode fiber using C-band only 16-QAM signals," *J. Lightw. Technol.*, vol. 42, no. 3, pp. 1136–1142, Feb. 2024. [Online]. Available: https://opg.optica.org/jlt/abstract.cfm?URI=jlt-42-3-1136
[26] P. J. Winzer and G. J. Foschini, "MIMO capacities and outage probabilities in spatially multiplexed optical transport systems," *Opt. Exp.*, vol. 19, no. 17, pp. 16680–16696, 2011. [Online]. Available: https://opg.optica.org/oe/abstract.cfm?URI=oe-19-17-16680
[27] K.-P. Ho and J. M. Kahn, "Mode-dependent loss and gain: Statistics and effect on mode-division multiplexing," *Opt. Exp.*, vol. 19, no. 17, pp. 16612–16635, 2011. [Online]. Available: https://opg.optica.org/oe/abstract.cfm?URI=oe-19-17-16612
[28] A. Andrusier, M. Shtaif, C. Antonelli, and A. Mecozzi, "Assessing the effects of mode-dependent loss in space-division multiplexed systems," *J. Lightw. Technol.*, vol. 32, no. 7, pp. 1317–1322, Apr. 2014.
[29] C. Antonelli, A. Mecozzi, M. Shtaif, and P. J. Winzer, "Modeling and performance metrics of MIMO-SDM systems with different amplification schemes in the presence of mode-dependent loss," *Opt. Exp.*, vol. 23, no. 3, pp. 2203–2219, 2015. [Online]. Available: https://opg.optica.org/oe/abstract.cfm?URI=oe-23-3-2203
[30] K. Shibahara et al., "Full C-band 3060-km DMD-Unmanaged 3-Mode transmission with 40.2-Tb/s capacity using cyclic mode permutation," *J. Lightw. Technol.*, vol. 38, no. 2, pp. 514–521, Jan. 2020.
[31] L. Dallachiesa et al., "Mode-group-Division multiplexing over a deployed 15-Mode-Fiber cable," in *2023 Opt. Fiber Commun. Conf. Exhib.*, 2023, pp. 1–3.
[32] G. Rademacher et al., "Characterization of the first field-deployed 15-Mode fiber cable for high density space-division multiplexing," presented at Proc. Eur. Conf. Opt. Commun., Basel, Switzerland, Sep. 18–22, 2022, Paper Th3B.1. [Online]. Available: https://opg.optica.org/abstract.cfm?URI=ECEOC-2022-Th3B.1
[33] G. Rademacher et al., "Random coupling between groups of degenerate fiber modes in mode multiplexed transmission," *Opt. Exp.*, vol. 21, no. 8, pp. 9484–9490, 2013. [Online]. Available: https://opg.optica.org/oe/abstract.cfm?URI=oe-21-8-9484
[34] C. W. Gardiner, *Stochastic Methods for Physics, Chemistry and Natural Sciences*. New York, NY, USA: Springer-Verlag, 1983.
[35] R. Ryf et al., "Transmission over randomly-coupled 4-core fiber in field-deployed multi-core fiber cable," in *2020 Eur. Conf. Opt. Commun.*, 2020, pp. 1–4.